Glacial Isostatic Adjustment Modelling for Crustal Motion in North America

by

Connor Brierley-Green
B.Sc., Simon Fraser University, 2019

A Thesis Submitted in Partial Fulfillment of the
requirements for the Degree of

MASTER OF SCIENCE

in the School of Earth and Ocean Sciences

We acknowledge and respect the lək̓ʷəŋən peoples on whose traditional territory the university stands and the Songhees, Esquimalt and W̱SÁNEĆ peoples whose historical relationships with the land continue to this day.

Glacial Isostatic Adjustment Modelling for Crustal Motion in North America

by

Connor Brierley-Green
B.Sc., Simon Fraser University, 2019

Supervisory Committee

Dr. Thomas S. James, Co-supervisor (Geological Survey of Canada, School of Earth and Ocean Sciences)

Dr. Lucinda Leonard, Co-supervisor (School of Earth and Ocean Sciences)

Dr. Kelin Wang, Committee Member (Geological Survey of Canada, School of Earth and Ocean Sciences)

Abstract

Due to the expansion and retreat of the large ice sheets that covered most of Canada and parts of the northern United States during the Last Glacial Maximum (LGM), the surface of North America presently exhibits vertical and horizontal crustal motion due to glacial isostatic adjustment (GIA). The purpose of this study was to explore the effects that Earth rheology parameters have on this crustal motion and to find a model that best fits the observations. The Earth is assumed to be spherically symmetric, and this thesis explores the effects of varying the Earth-model parameters and the general limitations of the laterally homogeneous approximation.

The GIA models used in this study are randomly generated from a wide range of Earth rheological parameters for a 3-layered mantle viscosity model with the spherically symmetric Preliminary Reference Earth Model (PREM) for continuous density and elastic parameters. The surface loading model is ICE6G_C. A new Earth response calculation method dubbed the hybrid method is presented to calculate as much of the normal mode response as possible while still being accurate and robust. The crustal motion predictions of the randomly generated GIA models were compared to the observed MIDAS velocity fields for selected Global Navigation Satellite System (GNSS) sites across North America. The goodness-of-fit was assessed through a Root-Mean-Square (RMS) calculation of the residual velocities.

Three types of best models were produced: one for minimizing the vertical crustal response residuals, one for the horizontal crustal response, and one for the combined vertical and horizontal response. The horizontal and combined response exhibited two optimal viscosity profile ranges that produced small residuals, with the global optimum transitioning between these two optimal ranges between 100 and 120 km thick lithospheres, while the vertical response's optimal viscosity profile range was relatively consistent across all tested lithosphere thicknesses. The optimal viscosity profile for the

vertical response was close to other previously published viscosity profiles like VM5a and VM7, and it was most similar to VM1. The horizontal and combined response viscosity profile before the 100 – 120 km transition was also similar to VM1, but after the transition the viscosity profile shifted substantially, with the parts of the viscosity profile changing by more than an order of magnitude.

The best vertical response was for a lithospheric thickness of 100 km. The horizontal and combined responses did not show a well-defined minimum until the viscosity profiles across the 100 – 120 km transition were extrapolated before and after the transition. With this extrapolation, both the horizontal and combined showed a minimum RMS residual at 100 km akin to the vertical response. Using 100 km thickness as the best model for all responses, the RMS of the residuals were 1.012 and 0.684 mm/yr for the vertical and horizontal response respectively and 1.303 (vertical) and 0.791 (horizontal) mm/yr for the combined response. For the null hypothesis (no GIA model), the RMS values of the observations were 3.244 and 1.321 mm/yr for the vertical and horizontal responses, respectively.

The vertical and horizontal crustal motions of the best combined response model are more similar to the crustal motions of the best horizontal response model than to the crustal motions of the best vertical response model, suggesting that the combined model favours the horizontal constraints over the vertical constraints. Despite the extensive search through Earth rheology, the residuals of the best models are still relatively large. This indicates the potential limitation of the spherically symmetric approximation and the need to incorporate lateral heterogeneity to produce an improved fit to the observations. It may also indicate that other processes, such as surface hydrological change, contribute significantly to the GNSS-observed crustal motion signal and would need to be considered in a future joint analysis.

Table of Contents

List of Tables

List of Figures

Acknowledgments

I would like to thank my supervisors, Dr. Thomas James and Dr. Lucinda Leonard. Tom, for your constant support and guidance throughout the entirety of this project. Without your guidance and expertise, this report would likely never of seen the light of day. Lucinda, for the thoughtful feedback for this report and for allowing me to help instruct some of your classes despite the lack of experience. Without your assistance, I probably would have never broadened my experiences to including actually leaving the office computer.

I would also like to thank Dr. Kelin Wang and Dr. John He of the Geological Survey of Canada. Kelin, for your questions and feedback for when I presented my work during the committee meetings and the Pacific Geoscience Center student presentations. Answering questions is a fantastic way to truly grasp any material and while also keeping me sharp and on my toes. John, for your constant support for the computing clusters that I connected to for this project. This projected would be noting but a pipe dream if it was not for the leo2p and modeling2 clusters and your consistent help with installing all number of packages that I requested.

I would also like to acknowledge the people behind the NRCan HPCO computing clusters. Without Dorval, the programs used for this thesis would have taken months to complete. The support from a number of staff through the 3+ years of this masters also made any changes to the Dorval HPC as painless as possible which greatly help to keep the project on track.

Finally, I would like to thank my family and friends for the continued emotional support throughout the entire program. To my mum and dad who would not so subtly force me to visit for long weekends to play games and feed both me and my dog with an ungodly amount of meat. To my friends that would help me relax of a long day of trying to find one bug in 1000+ lines of code only then to make fun of me for messing up in any games that we played.

Chapter 1: Introduction

1.1 Overview

Glacial Isostatic Adjustment (GIA) is the response of the Earth to the surface loading and unloading caused by fluctuations in the size of ice masses like ice sheets, ice caps, ice fields, and alpine glaciers (Dietrich et al., 2010; Elliott et al., 2010; Richter et al., 2016 DeGrandpre and Freymueller, 2019). The growth of the ice mass induces a large weight on the Earth's surface which causes isostatic depression due to the dispersion of the more viscous mantle. When the ice melts, the weight causing that depression is removed which allows the Earth to rebound back to its original position. Movement from GIA takes a considerable amount of time, so much so that many parts of the Earth's surface that were covered with ice during the Last Glacial Maximum (LGM) are currently experiencing crustal motion (Peltier, 1986; James and Ivins, 1998; Simon et al., 2016). This crustal motion and internal mantle flow affects a number of different geological and geophysical phenomena like gravitational changes (Lombard et al., 2007; Cazenave et al., 2009), sea-level changes (Coulson et al., 2021), induced earthquake activity (Steffen et al 2014; Ojo et al., 2021), and other local phenomena like the tilting of the Great Lakes (Koohzare et al., 2008; Lewis et al., 2021). These phenomena have significant impacts across a wide range of geophysical disciplines, making understanding and modeling GIA induced crustal motions extremely important. Isostatic displacement and rebound are functions of both the weight of the surface load and the rheology of the Earth. In order to predict GIA, one needs to model the changing surface load and the Earth's response to that change.

1.2 Earth Response

1.2.1 Incompressible Half Space

Starting with the Earth response model, if we first assume that the Earth rheology can be expressed as a semi-infinite Newtonian viscous fluid half-space within 1D, following Turcotte and Schubert (2002), an equation for determining the Earth mantle response to the removal of an ice load can be expressed as equation 1.1

$$w = w_m e^{-t/\tau_r}, \tag{1.1}$$

where w is the surface displacement, w_m is the initial displacement at $t = 0$, t is time, and τ_r is the characteristic time for the exponential relaxation. τ_r is given by equation 1.2

$$\tau_r = \frac{4\pi\mu}{\rho g \lambda}, \tag{1.2}$$

where λ is the wavelength of the load, ρ is the density of the mantle, g is the gravitational acceleration, and μ is the mantle viscosity. τ_r is a function that represents the time it takes for the surface displacement to relax back into the initial displacement. The mantle viscosity and the relaxation time have a linear relation, and as such the mantle viscosity has an inverse effect on the decay rate of the surface displacement. An increase/decrease in mantle viscosity will cause the decay rate to increase/decrease, taking more/less time for the surface displacement to relax into its original position. In contrast, the wavelength has a linear relation to the decay rate and as such has the exact opposite effect that the mantle viscosity does on the decay rate. This set of equations, though an approximation, shows that calculating displacement is dependent on information about the Earth rheology.

To show an example of these equations in practice, one can use relative sea level (RSL) data. RSL is a measurement of sea level relative to a land-based reference frame, in contrast to eustatic sea level

change that represents the global change in sea level by volume of water in the ocean. Today RSL is measured by tide gauges situated on the coasts. Vertical land motion is measured by Global Navigation Satellite Systems (GNSS) sites. The relative sea-level measured by tide gauges is a combination of the local sea surface height change and vertical crustal motion. Radiocarbon-dated organic material collected over a range of elevations from sites having a defined relationship with past sea levels provide a relative sea-level history over hundreds or thousands of years (Peltier, 2004).

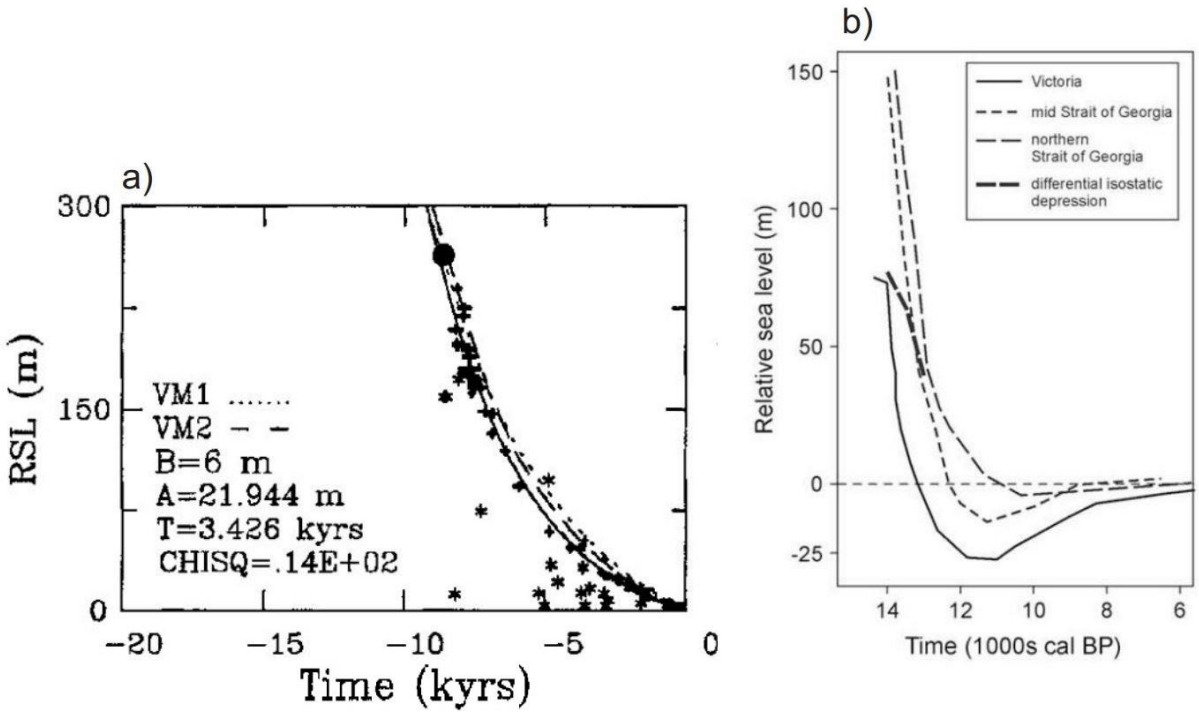

Figure 1.1: a) Relative sea-level (RSL) data from southeastern Hudson Bay and the predicted sea-level change for ICE-4G with the VM1 and VM2 viscosity profiles (Peltier, 2004). b) Three RSL curves at a set of locations near the Cascadia subduction zone (James et al., 2009); locations are shown in Figure 1.2.

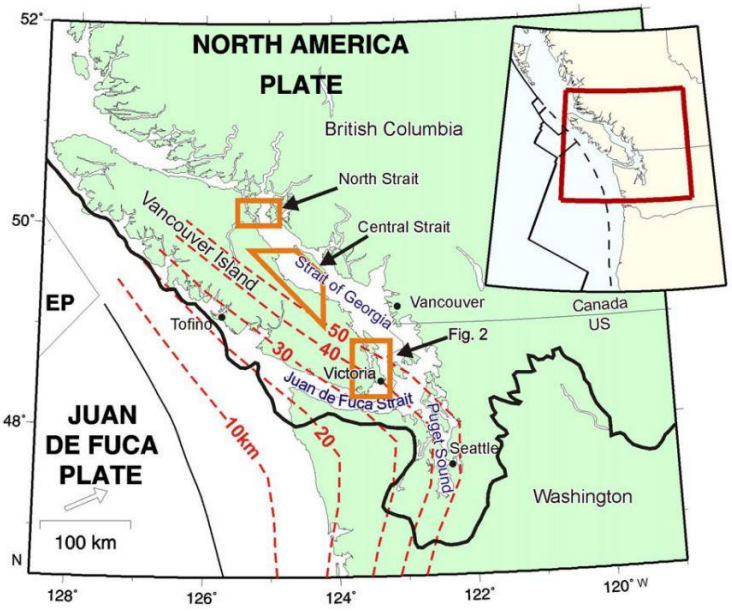

Figure 1.2: Location map for the RSL curves shown in Figure 1.1 b). Figure 1 of James et al., 2009.

The RSL curves from figure 1.1 can be used to estimate the underlying mantle viscosity. Peltier (2004) gives the decay time at $\tau_r = 3426$ years and a typical Laurentide Ice Sheet wavelength of $\lambda = 5000$ km (Turcotte and Schubert, 2002). ρ can be assumed to be an upper mantle density ($\rho = 3300$ kg/m^2). Equation 1.2 then leads to an approximate viscosity of $\mu = 1.39 \times 10^{21}$ Pa·s for the area around southeastern Hudson Bay.

Likewise, from the Cascadia subduction zone RSL curves, one can estimate that the decay time is approximately $\tau = 880$ years. The Cordilleran Ice Sheet was at its largest of around 900 km wide between 18 and 14 ka (Stumpf et al., 2000) and from figure 1.1, most of the change happened in the first 2000 years, and a rough estimate of the wavelength would be half of the width or $\lambda = 450$ km. With this, the approximation for the viscosity around the Cascadia subduction zone is $\mu = 3.22 \times 10^{19}$ Pa·s (James et al., 2000). There is a 2 order of magnitude difference between the two locations.

1.2.2 Maxwell Viscoelastic Model

Equations 1.1 and 1.2 offer a useful approximation, but do not represent realistic Earth structure. The Newtonian approach uses a purely viscous model which means that it is unable to incorporate any elastic response into the system. Instead, the Earth behaves more like a Maxwell viscoelastic material, with both viscous and elastic properties. A Maxwell solid has linear rheology characterised by three properties: rigidity, compressibility, and viscosity. With this, the Maxwell body is able to respond to the addition or removal of a load both elastically in the short term and viscously in the long term (James, 1991).

Maxwell viscoelastic motion can be simplified into a spring dashpot model, shown in figure 1.3, with the separate but connected elastic and viscous components (Bland, 1960).

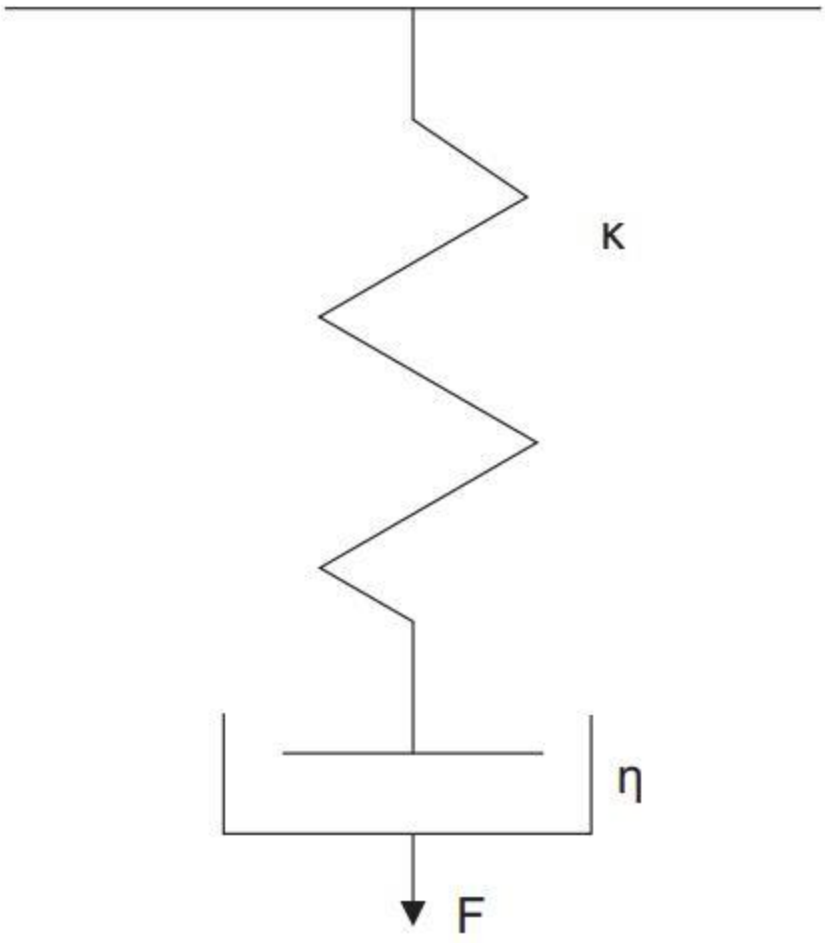

Figure 1.3: A Maxwell spring and dashpot model. This model is composed of a spring with constant, κ, connected to a dashpot with 1-D viscosity, η, with an applied force, F.

The total displacement of the system when an external force is applied is the sum of the displacement of the spring (the elastic component) and the dashpot (the viscous component) as expressed in equation 1.3.

$$d = d_{elc} + d_{vis} \tag{1.3}$$

The displacement from the applied force (F) is dependent on the system. For the elastic component, the equation is simply

$$F = kd_{elc}, \tag{1.4}$$

while the viscous component is expressed as

$$F = \eta \frac{dd_{vis}}{dt}, \tag{1.5}$$

where k is the spring constant and η is the 1-D viscosity. If the time derivative of equation 1.3 is taken, the resulting equation can be rewritten as

$$\frac{dd}{dt} = \frac{dF/dt}{k} + \frac{F}{\eta}, \tag{1.6}$$

and if the force is described as the delta function, then it can be expressed as

$$\frac{dd}{dt} = \frac{\delta'(t)}{k} + \frac{\delta(t)}{\eta}. \tag{1.7}$$

If this equation is integrated with the condition that if $t = 0^-$ then $d(t) = 0$, it can be rewritten as

$$d = \frac{\delta(t)}{k} + \frac{H(t)}{\eta} \tag{1.8}$$

with $H(t)$ being the Heaviside function. The response to a force that imposed at t=0 and maintained thereafter d_{heavy} is obtained from convolving 1.8 with a Heaviside function to result in

$$d_{heavy} = \frac{H(t)}{k} + \frac{t\,H(t)}{\eta}. \tag{1.9}$$

Equation 1.9 shows that the spring dashpot system has two components that react differently to an applied Heaviside force (James, 1991). The first component reacts instantaneously and is dependent on the spring constant. The second component linearly increases as a function of time, dependent on the viscosity, with no bound due to the lack of a restoring force. When an external force is applied, the elastic component immediately responds to the force, while the viscous component responds over time.

Likewise, when the force is removed, the elastic component will rebound back to its resting position instantly, while the viscous component will displace linearly.

This model gives a general explanation of how crustal motion from the ice mass removal is being observed. To express a method of solution for this, one can quantify a strain system which incorporates Maxwell viscoelasticity akin to the spring dashpot system shown in equation 1.10,

$$\varepsilon_{Maxwell} = \varepsilon_{Elastic} + \varepsilon_{Viscous}, \tag{1.10}$$

where ε is the strain for the Maxwell, elastic, and viscous system. From this, a stress tensor can be derived that incorporates the viscoelastic nature of the Maxwell spring dashpot system and incorporated into the conservations equation. The conservation equations are

$$\overline{\rho_1} = -\bar{\nabla}(\rho_0 \bar{s}), \tag{1.11}$$

for the conservation of mass,

$$\bar{\nabla}^2 \overline{\phi_1} = 4\pi G \overline{\rho_1}, \tag{1.12}$$

for the incremental gravitational potential, and

$$0 = -\frac{\rho_0 \bar{\nabla}\phi_0}{\bar{s}} - \bar{\rho}_1 \bar{\nabla}\phi_0 - \rho_0 \bar{\nabla}\bar{\phi}_1 + \bar{\nabla} \cdot \underline{\bar{T}}, \tag{1.13}$$

for the momentum equation, where ϕ is the gravitational potential, ρ is the density, G is the gravitational constant, s is the displacement, and $\underline{\bar{T}}$ is the Laplace-transformed total stress. Linearizing these equations results in the momentum equation:

$$0 = -\bar{\rho}_1 \bar{\nabla}\phi_0 - \rho_0 \bar{\nabla}\bar{\phi}_1 - \bar{\nabla}(\bar{u}\, \rho_0 g_0) + \bar{\nabla} \cdot \underline{\bar{T}}_{Maxwell}, \tag{1.14}$$

where g_0 is the gravitational acceleration, $\bar{u}$ is a displacement vector, and $\underline{\bar{T}}_{Maxwell}$ is the incremental Maxwell viscoelastic stress tensor (Backus, 1967; Peltier, 1974; Wu and Peltier, 1982; James, 1991). The

solutions to these equations can be obtained through a number of different numerical methods, including methods that assume the Earth's rheology to be laterally homogeneous and numerical methods that provide the response for Earth models with lateral heterogeneity. Chapter 2 will discuss further how one solves these equations with a laterally homogeneous Earth rheology.

An example of the difference between the Maxwell body response and the Newtonian model response is shown in figure 1.4.

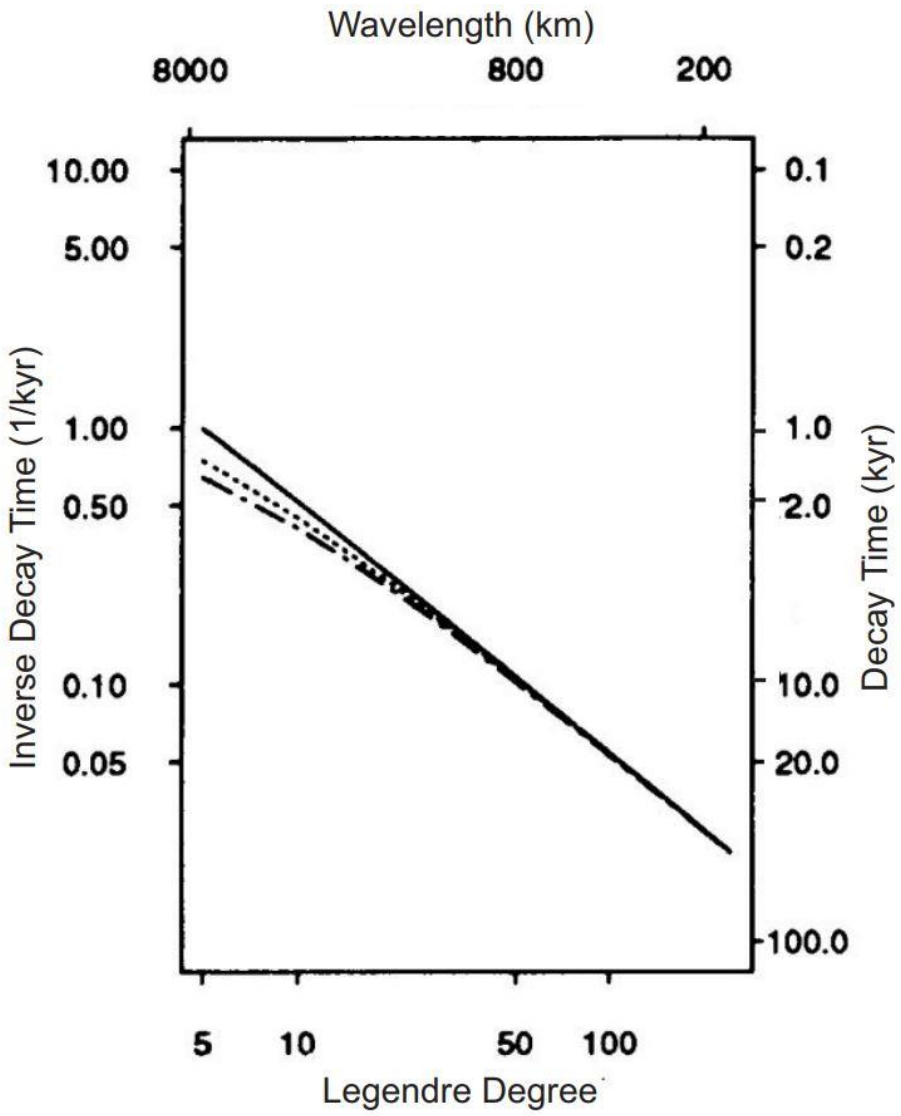

Figure 1.4: Decay times for a uniform Maxwell sphere (dot-dashed line), a uniform viscous sphere (dashed line) and a viscous half space (solid line). Parameters used to create this figure are described in figure 5 of James, 1991.

In the low Legendre degrees, there is a notable difference between the Newtonian viscous half space and the Maxwell sphere, while at higher degrees, the two models predict the same decay times. This is due to the addition of the elastic component of Maxwell model observing a stronger initial decay in the short term while the viscous half space has a consistent decay time throughout the degrees.

1.3 Surface Loading

The force applied in the case of GIA comes from the surface load. The surface load comprises all the redistributed weight on the Earth's surface, mainly from expanded ice sheets, with concomitant reduction in ocean water mass. During the Last Glacial Maximum, three major ice sheets covered the vast majority of Canada and parts of the northern United States: the Cordilleran Ice Sheet, the Innuitian Ice Sheet, and the Laurentide Ice Sheet. To discern how these ice sheets affected the surface loading, one needs to know their extent and thickness. Many studies seek to answer this question, and for this analysis, the ICE6G_C model will be used as the model for ice extent and thickness (Peltier et al., 2015). The extent of the North American portion of the ICE6G_C model, and thicknesses at specified times, are shown in figures 1.5 and 1.6, respectively.

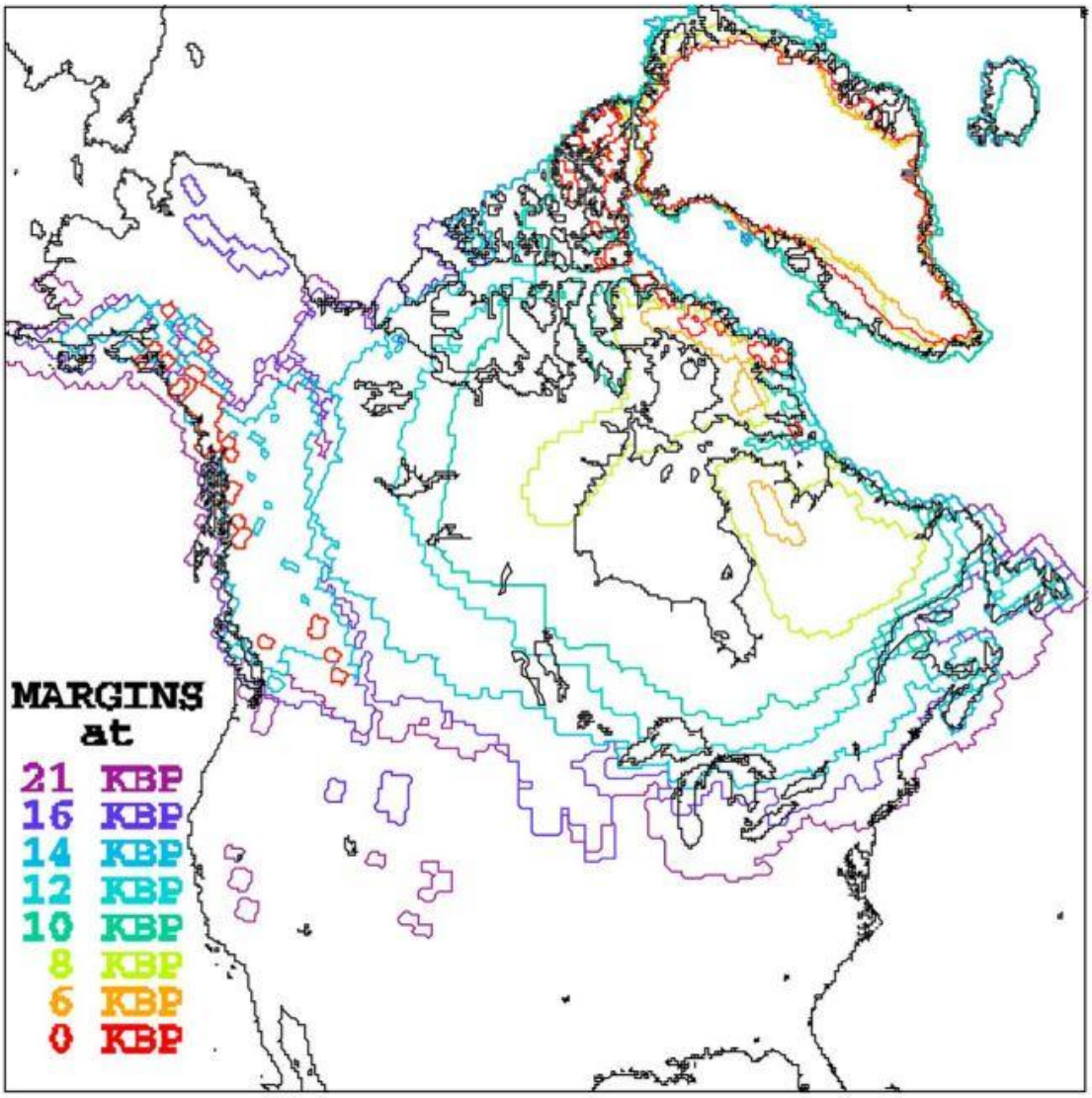

Figure 1.5: The extent of the ICE6G_C ice loading model for North America and Greenland. The colours refer to the extent at different times denoted on the legend, KBP referring to kyr before present. Figure 3 of Peltier et al., 2015.

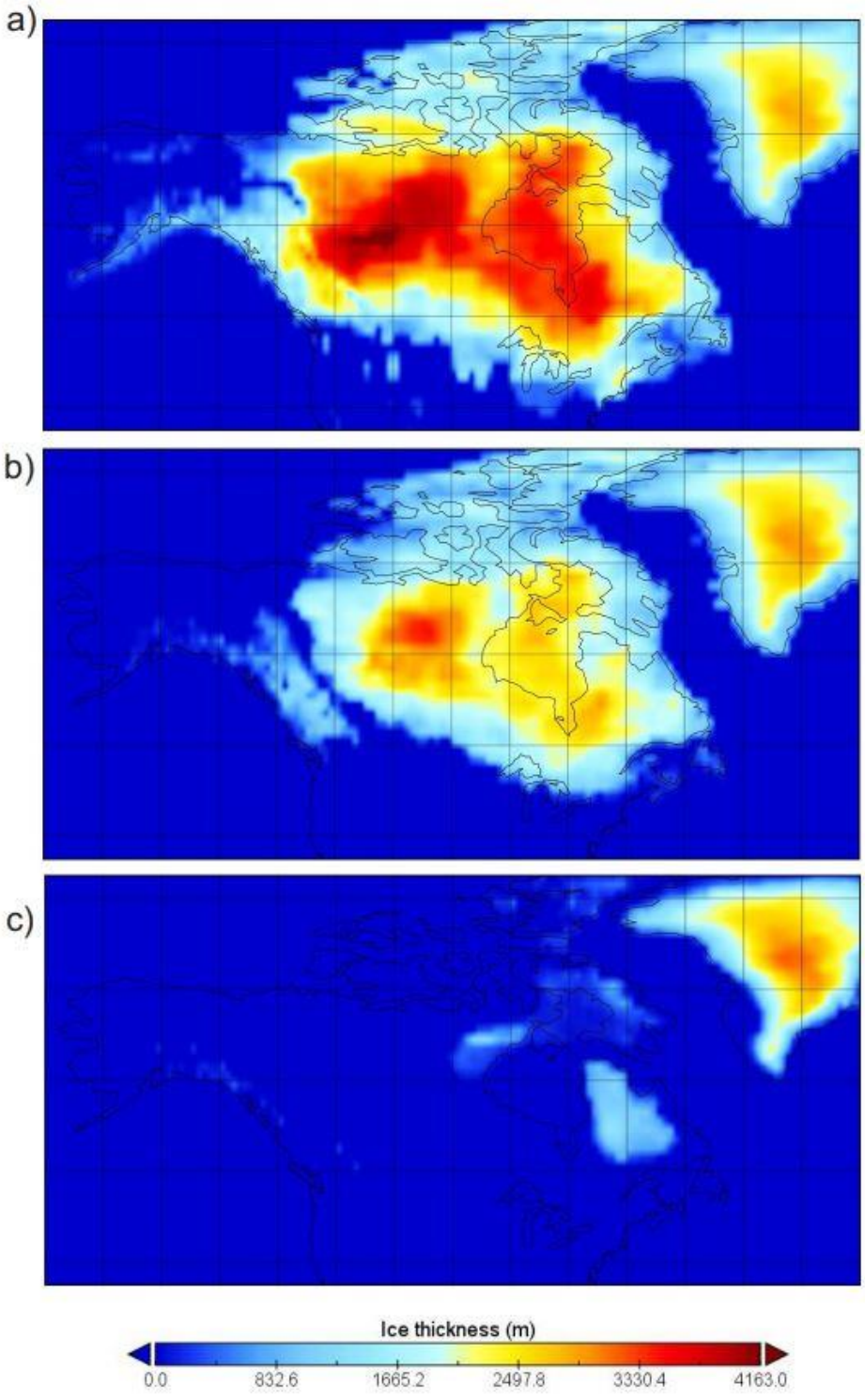

Figure 1.6: Maps of ice thickness for North America and Greenland at 21 ky (a), 14 ky (b), and 8 ky (c). Colour scale is consistent for all maps. Data and program used to generate figures from https://www.atmosp.physics.utoronto.ca/~peltier/data.php

The changing ice mass is the major contributor to surface loading, but it is not the only source. Another component of the surface load for coastal regions is the ocean itself. The variation in the ice mass and the respective Earth response is relatively straightforward regarding the ice mass changing the Earth's displacement. If the ice mass increases, depression occurs; if the ice mass reduces, rebound occurs.

Sea-level variations are non-uniform and depend on several different processes. The variations significant to GIA are the displacement caused by ice load changes and the gravitational effect of the ice mass (Woodward, 1888; Mitrovica and Peltier, 1991a; Mitrovica and Milne, 2003). Due to the gravitational attraction of the ice load, the sea level near the ice mass will increase. This higher sea-level comes with more weight from excess water. This weight adds to the surface load induced, thus causing a stronger depression. When deglaciation occurs, the ice mass decreases, the gravitational attraction is reduced, and the nearby sea level falls, thus removing some of the weight of the ocean and leading to further reduced surface loading. This phenomenon is called ocean loading and is the theory for how the ocean is redistributed during glaciation to maintain gravitational equipotential. To include the ocean loading effect into the surface load, one requires knowing the sea level as a function of time.

The sea level equation, regarding GIA, can be expressed as

$$SL(\theta,\psi,t) = -U(\theta,\psi,t) + N(\theta,\psi,t) + c(t), \tag{1.15}$$

where SL is the sea level, U is the vertical crustal displacement, and N is the vertical geoid position, all defined at time t and at a set of spatial coordinates θ and ψ. c is a term that constrains the conservation of mass. For a more complete solution for the evolution of the sea level, this can be expanded following Farrell and Clark (1976) to

$$\Delta SL(\theta,\psi,t) = \frac{\rho_i}{g_o} G_\phi(\theta,t) * I(\theta,\psi,t) + \frac{\rho_w}{g_o} G_\phi(\theta,t) * \Delta SL(\theta,\psi,t) O(\theta,\psi,t) + c(t). \tag{1.16}$$

ΔSL is the change in sea level, G_ϕ is the Green's function for the gravitational potential (as described in Peltier, 1974), I is the ice loading function, $*$ denotes convolution in time and space for the respective terms, ρ_i and ρ_w are the densities of ice and water, g_o is the gravitational acceleration, and O is the ocean function

$$O(\theta,\psi,t) = \begin{cases} 1, & Ocean\ exists \\ 0, & No\ ocean\ exists \end{cases}. \tag{1.17}$$

c represents the geographically uniform shift in the geoid that is constrained by invoking the conservation of mass which is shown in equation 1.15:

$$c(t) = -\frac{M_I(t)}{A_O\rho_w} - \frac{1}{A_O}\langle\frac{\rho_i}{g_o}G_\phi(\theta,t) * I(\theta,\psi,t) + \frac{\rho_w}{g_o}G_\phi(\theta,t) * \Delta SL(\theta,\psi,t)O(\theta,\psi,t)\rangle_O\,. \tag{1.18}$$

M_I is the change in the ice mass, A_O is the area of the ocean, and $\langle\ \rangle_o$ represents the integration limit to the location of the ocean (Peltier, 1974; Farrell and Clark, 1976; Mitrovica and Milne, 2003; Simon, 2014). Equation 1.16 shows two essential observations. First, the sea-level change depends on itself since it appears on both sides of the equation. Second, there is a convolution between the gravitational potential and the ice loading function, meaning that there is a blending of the two functions, representing how the ice load induces local gravitational attraction. Equation 1.16 and a model representing the change in ice mass over time provide a method of predicting and calculating relative sea level and the ocean loading effect which then can be included into the surface loading model.

1.4 Horizontal Crustal Motion

Though the theory behind Earth response models and surface loading models was well understood, there were a number of limitations in the past that hampered GIA modeling. The traditional GIA observational tools recorded vertical land motions from measuring relative sea level from coastal and lake side sites. Not only did these calculations require a number of physical sites and multiple

corrections, but this type of data collection would also only give information on the vertical crustal motion (James and Morgan, 1990; Carrera et al., 1991; Sella et al., 2007). Once space geodetic techniques were introduced in the early 1990s, a means of measuring both vertical and horizontal motions was available which allowed for the modeling and analysis of horizontal crustal motions.

Global Navigation Satellite Systems (GNSS) sites monitor crustal motion in 3 dimensions while being accurate to less then a millimetre per year (Sella et al., 2007; Kreemer et al., 2018). Satellite geodetic methods not only recorded horizontal crustal motions, but also expanded the vertical datasets, allowing for vertical motions to be recorded inland. With this new GNSS data, GIA horizontal motion was successfully observed and modeled for Fennoscandia (Milne et al., 2001). The same types of studies were also done in North America, but an accurate GIA model was not found for North America due to not finding an adequate Earth and ice loading model (James and Lambert, 1993; Mitrovica et al., 1993, Sella et al., 2007). There are more sites across Canada now, an example being the IGS14 crustal motion observation data set from the MIDAS database shown in figure 1.7 (Blewitt et al., 2018; Robin et al., 2020); however, there is still a struggle to find a GIA motion model that accurately matches the observed horizontal and vertical crustal motions akin to the one available for Fennoscandia.

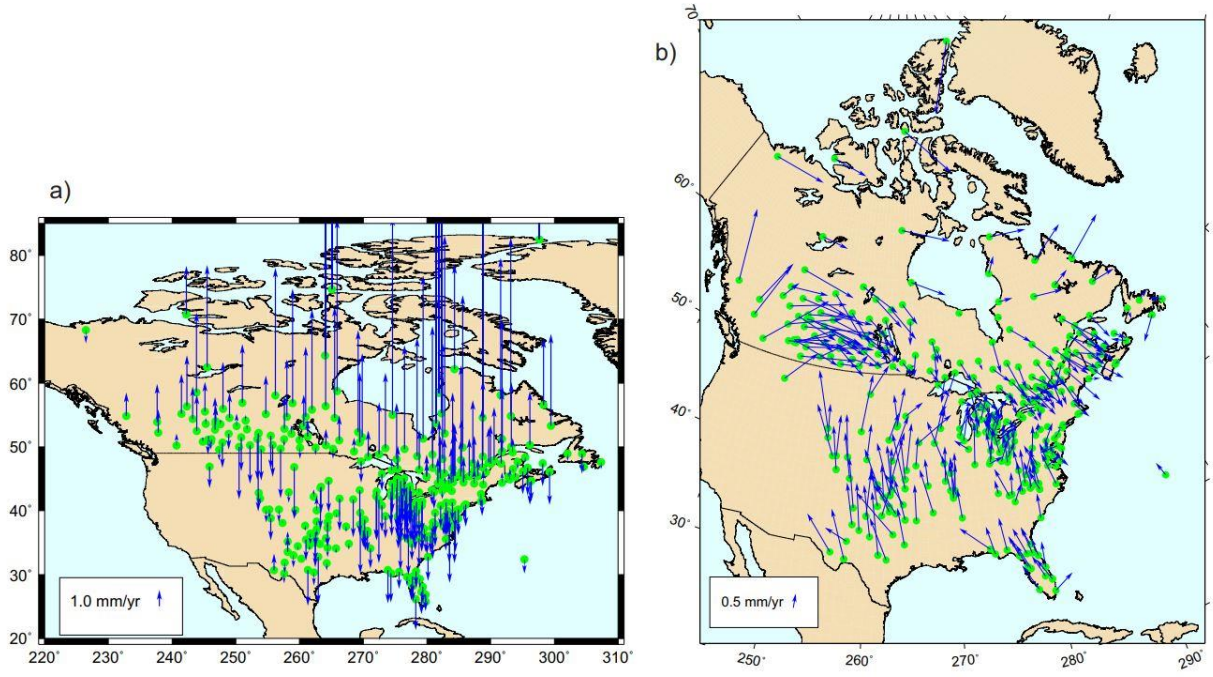

Figure 1.7: Crustal motion maps from the IGS14 MIDAS dataset for North America. (a) A grid of vertical crustal motions. (b) Horizontal crustal motions for a number of GNSS sites across North America. The horizontal data are set to the NA reference frame (Kreemer et al., 2014).

1.5 Thesis Scope and Organization

GIA modeling is usually focused on finding a number of model constraints, such as the viscosity of the mantle layers, the effective thickness of the elastic lithosphere, and the extent and thickness of the ice mass as it expanded and retreated. This is encapsulated in an Earth response model and a surface loading model. This thesis aims to explore the effects of changing key parameters in the Earth response model on the fit to observed vertical and horizontal motions across North America.

The geographical scope is limited to eastern and central North America, and it avoids the tectonically active western margin. The Earth models were generated by randomly creating viscosity profiles for a number of defined lithospheric thicknesses. This random approach permits a statistically uniform coverage of parameter space and avoids potential biases to other well-documented viscosity profiles like VM1, VM5a, and VM7 (Peltier et al., 1976; Argus et al., 2014; Roy et al., 2017).

The Earth models are kept spherically symmetric. This symmetry is required for the use of numerical methods of generating Earth response models that are not computationally demanding. This approach allows more models to be generated and, thus, a more complete examination of parameter space can be made. The ice loading model is kept consistent, utilizing the ICE6G_C ice loading model (Argus et al., 2014; Peltier et al., 2015) and programs for including the ocean loading effect (Simon, 2014). With the GIA models, one can find what parameters produce the best model through an observational data set provided by a number of GNSS sites across Canada and the United States shown in figure 1.7.

The following two chapters dive deeper into the process of creating the Earth response models and the results of comparing the GIA models to the observational data set. Chapter 2 introduces an improved method developed for calculating Earth response, dubbed the hybrid normal mode-collocation method. This chapter extensively compares this new method and other well-documented methods that use the spherically symmetric approximation to show that the hybrid method can produce accurate Earth models while reducing the effects of the documented issues present in the other methods. Chapter 3 compares GIA model predictions to GNSS observations of crustal motion for selected Earth models and assesses the best fit through a range of lithospheric thicknesses. Finally, the summary chapter discusses the optimal fit of models to data, the remaining data-model residuals, and makes suggestions for next steps.

Chapter 2: A Hybrid Normal Mode-Collocation Method for Finding the Response of Laterally Homogeneous Compressible Maxwell Viscoelastic Earth Models

2.1 Introduction

Glacial Isostatic Adjustment (GIA) is the response of the solid Earth to the surface loading and unloading caused by fluctuations in the size of ice masses. Earth models utilized in GIA modelling generally possess a constrained elastic and density structure (Peltier, 1974; Wu and Peltier, 1982; Mitrovica and Peltier, 1992; Tamisiea et al., 2002; Klemann et al., 2003; Tanaka et al., 2006; Tanaka et al., 2009; Roy et al., 2018). A number of methods have been described and utilized to derive the surface-loading response of both laterally homogeneous (i.e., spherically-symmetric) and laterally heterogeneous viscoelastic spherical Earth models for a variety of linear and non-linear rheologies (Steffen et al., 2006; Peltier et al., 2015; Li et al., 2018). When lateral heterogeneity or a non-linear rheology is considered, usually computationally-intensive finite element (Martinec, 2000; Zhong et al., 2003; Wu et al., 2006; Tanaka et al., 2011; Hampel et al., 2019) or finite volume methods (Tromp et al., 1999; Latychev et al., 2005b) determine the surface-loading response. These methods are capable of incorporating laterally varying features of Earth structure, such as ocean-continent variations in lithospheric thickness and spatial variations in mantle viscosity, which vary by orders of magnitude between sub-cratonic and active plate boundary regions.

Laterally homogeneous Earth models are still, however, broadly utilized in GIA modelling. They offer established and benchmarked (Spada et al., 2011; Martinec et al., 2018) techniques for rapidly scanning wide ranges of values of Earth model parameters, such as lithospheric thickness or the viscosity of a layered mantle. For regional studies, they derive Earth structure parameter values that can be

compared and contrasted globally to other regions, thus providing foundational information for more complex three-dimensional Earth models.

The focus of this chapter is on a class of laterally-homogeneous linear viscoelastic spherical Earth models having a compressible Maxwell viscoelastic rheology and introduce a new robust method for finding the surface loading response. The chapter is structured by first discussing the theory of the response of linear Maxwell Earth models to surface loading. The responses obtained from several previously described methods (Mitrovica and Peltier, 1992) are described and their advantages and shortcomings highlighted. Finally, then introducing and discussing a new method that is numerically stable, provides a physically robust response, and that can be readily automated to generate surface-loading responses for a suite of Earth models.

2.2 Theory

An Earth model, in the context of GIA, is a model of the variation in density, elastic parameters, and flow properties (often expressed as a linear viscosity) of the Earth. The model determines how the Earth responds to surface or gravitational loading. To find the surface loading response, the equations of motion (conservation of mass and momentum and Poisson's equation for gravitational potential) are linearized in the Laplace transform domain in terms of the vertical displacement U_n, horizontal displacement V_n, and gravitational potential $\phi_{1,n}$. The response is found for each spherical harmonic degree n through a separation of variables, which leads to six coupled first-order ordinary differential equations that are numerically integrated from the core to the surface of the Earth. To incorporate Maxwell viscoelasticity, it is convenient to carry out calculations in the Laplace transform domain with Laplace transform parameter s. Frequently, the response is written in terms of non-dimensional quantities called Love numbers (Wu and Peltier, 1982).

$$\begin{bmatrix} U_n(r,s) \\ V_n(r,s) \\ \phi_{3,n}(r,s) \end{bmatrix} = \phi_{2,n}(r) \begin{bmatrix} \frac{h_n(r,s)}{g_0} \\ \frac{l_n(r,s)}{g_0} \\ -k_n(r,s) \end{bmatrix} \tag{2.1}$$

$$\phi_{1,n} = -\phi_{2,n} + \phi_{3,n} = -\phi_{2,n}(1 + k_n) \tag{2.2}$$

In these equations g_o is the gravitational acceleration at the Earth's surface, s is the Laplace transform parameter, having units of inverse time, $\phi_{2,n}$ is the gravitational potential of the imposed surface load, $\phi_{3,n}$ is the gravitational potential of the deformed Earth, $\phi_{1,n}$ is the total perturbation to the gravitational potential, r is radius, and h_n, l_n, and k_n are the corresponding Love numbers for vertical and horizontal displacement and gravitational potential. The Love numbers can be expressed as a function of s, the inverse decay time, for each spherical harmonic degree. The vertical Love number $h_n(s)$ can be expressed

$$h_n(s) = \frac{Q_n(s)}{\det M_n(s)} + h_{elc} \tag{2.3}$$

where $h(s)$ is the s-dependent Love number, h_{elc} is the elastic limit of the Love number (as $s \rightarrow \infty$), $Q(s)$ is a weighted sum of the first element of the three propagated vectors based on boundary conditions, and $M(s)$ is a matrix that contains 6 linearly independent solutions to the equations of motion (see Peltier, 1974, for a complete discussion). By utilizing the Cauchy residue theorem and the assumption that the singularity poles are simple poles, equation 2.3 can be expressed as

$$h_n(s) = \sum_{j=1}^{N} \frac{r_j^n}{s + s_j^n} + h_{elc}. \tag{2.4}$$

Where N is number of modes and the response amplitudes r_j^n are

$$r_j^n = \frac{Q_n(-s_j^n)}{\frac{d}{ds}\left(\det M(s)\right)|_{s=-s_j^n}} \tag{2.5}$$

The decay times (poles) s_j^n occur along the negative s-axis where $\det M(s) = 0$. From (2.4), the infinite-time ($\lim_{s\to 0} s$) viscoelastic response is

$$h_n(t = \infty) - h_{elc} = \sum_{j=1}^{N} r_j^n \Big/ s_j^n \tag{2.6}$$

assuming that $s_j^n > 0$ and that $h_n(t = \infty)$ represent the isostatic limit, h_{iso}.

In the time domain, the inverse Laplace transform of equation 2.4 gives

$$h_n(t) = \sum_{j=1}^{N} r_j^n e^{-s_j^n t} + h_{elc}\delta(t). \tag{2.7}$$

The response of the Earth model is thus a set of inverse decay times and corresponding amplitudes that describe the response in either the Laplace-transform s domain (2.4) or the time t domain (2.7). The elastic response h_{elc} and isostatic limit h_{iso} can be directly calculated (e.g., Wu and Peltier, 1982) and equation 2.6 provides a way to determine the completeness of the modal solution. It is convenient to define the infinite-time modal amplitude (MA) r_j/s_j as a percentage of the difference between the isostatic and elastic response

$$MA\ (\%) = \left(\sum_{j=1}^{N} \frac{r_j}{s_j} \Big/ (h_{iso} - h_{elc}) \right) 100\%. \tag{2.8}$$

A given mode can be identified as carrying a substantial or minor fraction of the Earth model response. The 6 first-order coupled differential equations incorporate 4 s-dependent viscoelastic parameters $\beta(s)$, $\gamma(s)$, $\mu(s)$, and $\lambda(s)$ that arise in the separated equations of motion (James, 1991).

$$\beta(s) = \frac{(\lambda + 2\mu)(s + \frac{\mu K}{\eta(\lambda + 2\mu)})}{s + \mu/\eta} \tag{2.9}$$

$$\gamma(s) = \frac{3K\mu s}{(\lambda + \mu)(s + \frac{\mu K}{\eta(\lambda + \mu)})} \tag{2.10}$$

$$\mu(s) = \frac{\mu s}{s + \mu/\eta} \tag{2.11}$$

$$\lambda(s) = \frac{s\lambda + \mu K/\eta}{s + \mu/\eta} \tag{2.12}$$

$$K = \lambda + 2\mu/3 \tag{2.13}$$

where η is viscosity and three linearly dependent elastic parameters are rigidity μ, compressibility K, and λ. In searching for modes along the negative s-axis, when the inverse decay time is equal to $-\mu/\eta$, $-\mu K/\eta(\lambda + 2\mu)$, or $-\mu K/\eta(\lambda + \mu)$ at some radius r, the viscoelastic parameter is singular. In practice, the numerical integration of the separated equations of motion utilized by the full normal mode analysis (FNMA) generally delivers a solution, but derived modes may be erroneous, or modes may not be found (Peltier, 1974; Wu and Peltier, 1982). To address these issues, two alternative methods, pure and mixed collocation, have been proposed to find the response in the Laplace transform domain.

While the FNMA directly determines the response amplitude, the collocation methods determine the amplitudes through numerical techniques. Since the Love numbers may be evaluated for arbitrary values of s, one can determine the response amplitude for a given inverse decay time from the response $h_n(s)$ (2.4) along the positive axis of s (Mitrovica and Peltier, 1992). A least-squares solution solves the response amplitudes for a given set of inverse decay times.

The pure collocation method uses arbitrary inverse decay times. The inverse decay times are picked equally spaced in log(s) space, but the range of inverse decay times and the density of points can

be chosen for the given model (Peltier, 1974). This results in a revision of equation 2.4 where the normal modes are replaced with a set of evenly spaced inverse decay times, S_j^n, and the normal mode response amplitudes would be replaced with the response amplitudes , R_j^n for S_j^n which are placeholders for the synthetically chosen "modes" and their corresponding response amplitude.

$$h_n(s) = \sum_{j=1}^{N} \frac{R_j^n}{s + S_j^n} + h_{elc}. \tag{2.14}$$

The pure collocation method is a curve fitting method. The least-squares solution finds the best values for R_j^n given S_j^n that will match $h_n(s)$.

For the mixed collocation method, the inverse decay times are chosen to be the FNMA decay times. The amplitudes of the normal mode inverse decay times are determined through a least-squares solution, similar to the pure collocation method. The mixed collocation method depends on the normal modes that can be found, and if major modes are missing the method may not fit the directly calculated Love number very well.

2.3 Comparison of Existing Methods

To compare and illustrate the differences between the three methods for a specific Earth model and spherical harmonic degree (n=8 chosen), the PREM density and elastic parameter Earth model (Dziewonski and Anderson, 1981) approximated with 163 layers, and the VM5a viscosity structure (Peltier et al., 2015) (Figure 2.1) were utilized.

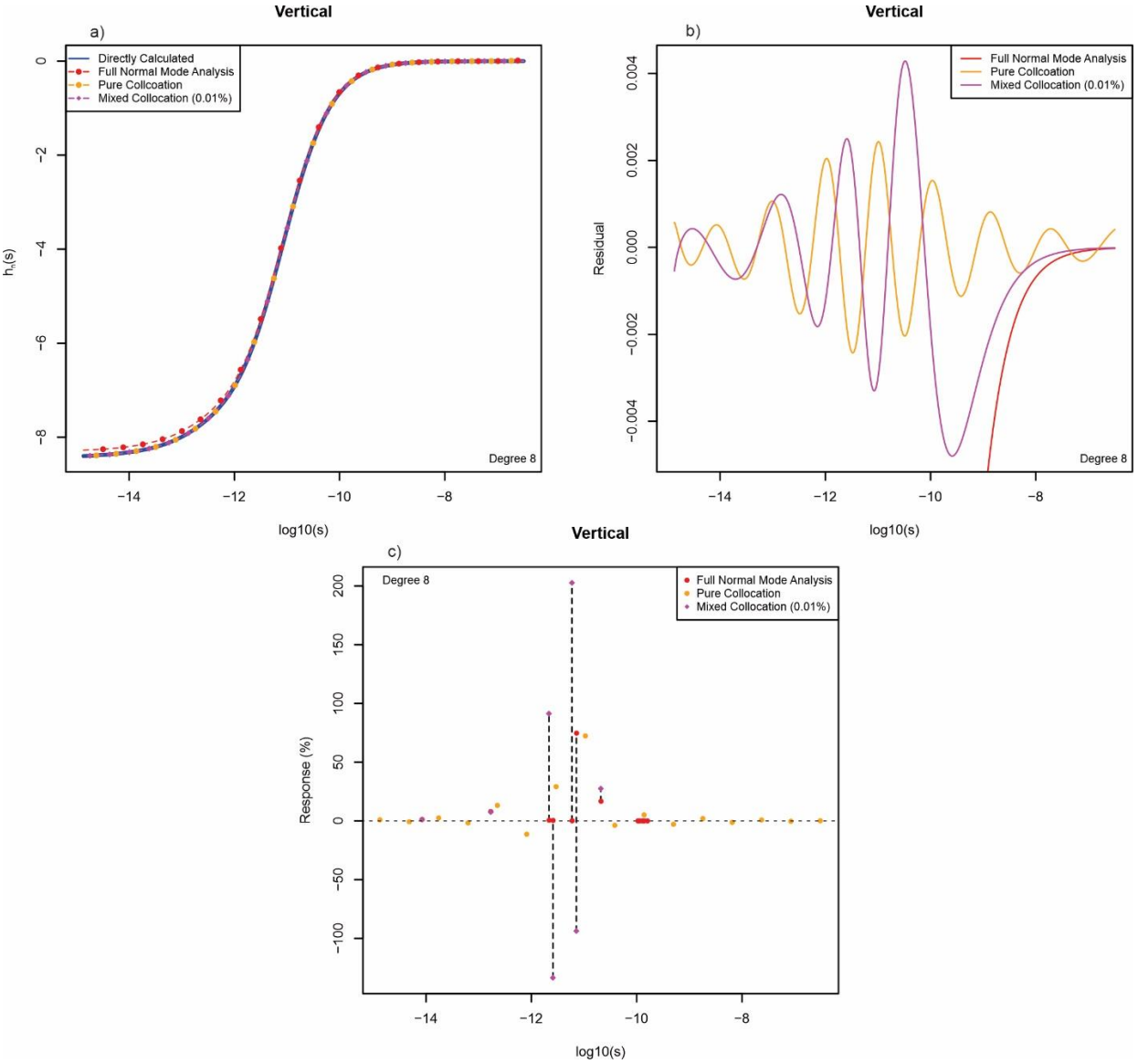

Figure 2.1: For spherical harmonic degree 8, the (a) directly-computed s-dependent vertical response Love number $h_n(s)$ and the corresponding responses for the FNMA method, pure collocation, and mixed collocation methods are given. (b) Residuals of the FNMA, pure collocation, and mixed collocation methods relative to the directly calculated vertical Love number $h_n(s)$. The scale is chosen to focus on the pure and mixed collocation results, as the FNMA has significantly larger residuals. (c) Vertical response amplitudes, expressed as a percentage of the viscoelastic component of the infinite-time (fluid) response (equation 2.8). The FNMA and the mixed collocation methods share the same inverse decay times, and the amplitudes are joined by vertical dotted lines to illustrate the large differences. The VM5a viscosity profile (Peltier et al., 2015) is assumed and the PREM density and elastic parameter structure is utilized (Dziewonski and Anderson, 1981).

The three methods agree well with the directly calculated Love number (Figure 2.1a), although the FNMA curve visibly departs from the directly computed Love number $h_n(s)$ at small s. At the elastic

limit, the directly calculated Love numbers are accurate to 5 significant figures (Dahlen, 1976). Numerical issues arose when approaching the fluid limit, which was avoided by retreating 5 points away from the first point showing numerical instability. The residuals (Figure 2.1b) and the amplitudes of specific inverse decay times differ (Figure 2.1c), sometimes significantly. The pure collocation method generates the smallest residuals (Figure 2.1b), indicating that it reproduces the directly calculated Love number most accurately, while the mixed collocation method performs nearly as well. In contrast, the FNMA method has residuals that are significantly larger than the two collocation methods. This suggests that the collocation methods are superior, but Figure 2.1c shows that both collocation methods produce modal amplitudes that may be physically unrealistic.

Both collocation methods produce responses with negative amplitudes, which is thought to be physically unrealistic, as it would lead to generating uplift, rather than subsidence, in response to imposition of a surface load. The mixed collocation method was implemented only using inverse decay times that generated a modal amplitude larger then 0.01% to avoid having a large number of closely spaced decay times that could lead to numerical instabilities in the least squares inversion. Nevertheless, the mixed collocation method also produces some responses with amplitudes larger than 100%. This would suggest that the inverse decay time carries more than the total viscoelastic response of the degree. This large positive amplitude of one is counterbalanced by a nearby response that carries a similar magnitude negative amplitude. The behaviour is likely caused by the close spacing (in inverse decay time s) of the FNMA normal modes, thus making the least-squares process poorly conditioned. Despite this behaviour, which appears to be physically unrealistic, the collocation methods do reproduce the directly-computed Love number well, with the residuals being about 3 orders of magnitude smaller than the computed Love number.

To determine the impact of these effects on a geodetically-measurable quantity, present-day crustal uplift rates were computed for the three methods (Figure 2.2), using the ICE6G_C global loading

model (Peltier et al., 2015), PREM density and elastic parameter Earth model (Dziewonski and Anderson, 1981), and the VM5a viscosity profile (Peltier et al., 2015) (Figure 2.2). Summation was carried out from degrees 1 to 256.

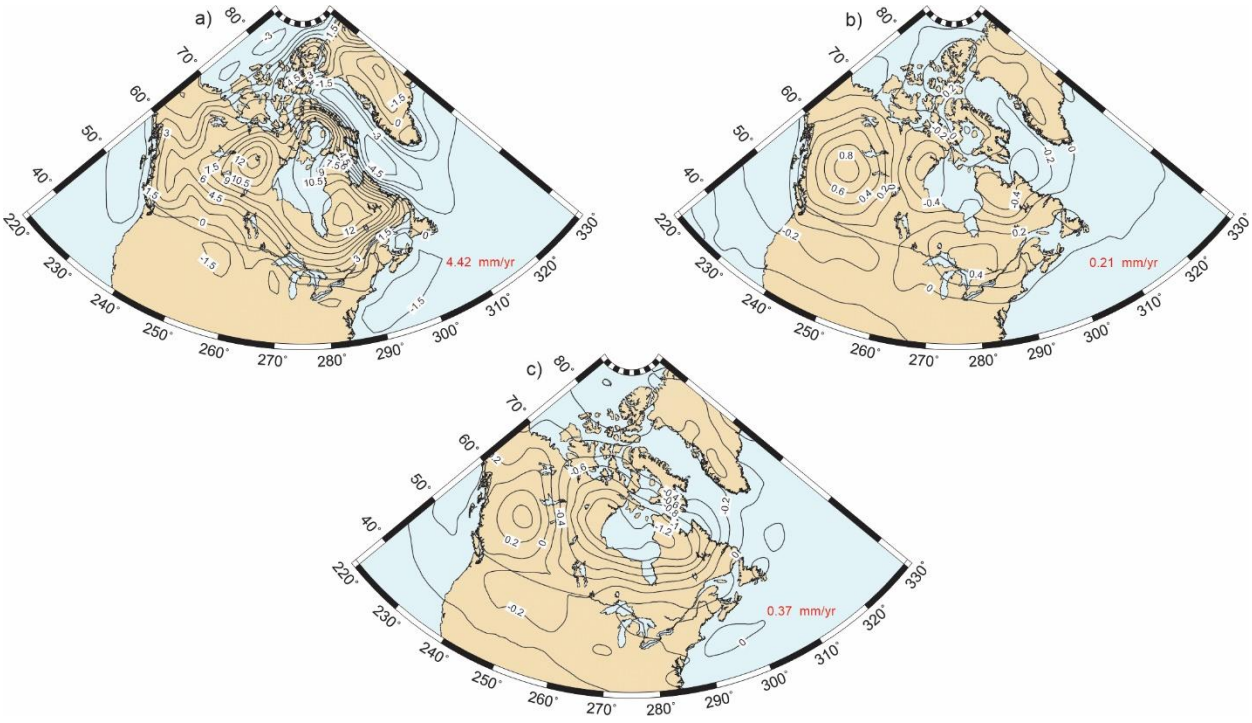

Figure 2.2: (a) Predicted crustal uplift (in millimetres per year) for North America using the ICE6G_C ice load and VM5a viscosity structure (Peltier et al., 2015) for the pure collocation method, and the difference between the pure collocation method and (b) FNMA and (c) mixed collocation methods, respectively. The numerical value on each map represents the Root Mean Square (RMS) of the (a) uplift or (b and c) uplift difference within the displayed region. Summation was carried out from degree 1 to 256.

Using the responses derived from the Pure Collocation method as the reference (Figure 2.2a) (root-mean-square (RMS) uplift rate of 4.4 mm/yr), the differences with the FNMA (Figure 2.2b, RMS difference of 0.21 mm/yr) and mixed collocation methods (Figure 2.2c, RMS difference of 0.37 mm/yr) were determined. These differences are substantial and expressed as percentages amount to about 5% (FNMA) and 8% (mixed collocation). The absolute value of the largest differences with the pure collocation method exceed 0.8 mm/yr (FNMA) and 1.2 mm/yr (mixed collocation). The differences

highlight how the methods, despite having good agreement to the directly-computed vertical Love numbers for the two collocation methods (results for all degrees were inspected) and relatively small residues, can result in uplift rate predictions that vary substantially, with a 1 mm/yr difference being larger than the error of the GNSS sites (Sella et al., 2007; Kreemer et al., 2018). Given the variation in the computed uplift rates and the issues the methods have with finding physically-realistic modal amplitudes while generating good agreement with the directly-computed vertical Love numbers, it would be desirable to develop a method that removes or reduces these issues. Here the hybrid normal mode-collocation method (HNMC, here termed the hybrid method) is introduced and compared to the methods described above.

2.4 Hybrid Normal Mode-Collocation Method

The hybrid method finds the FNMA modes and amplitudes, and then applies the pure collocation method on the residual $h_n(s)$-series. It is carried out in the following steps:

1: Find the normal modes via the FNMA.

2: Cull the modes that carry less then a specified percentage of the total response (this chapter using 0.01%)

3: Calculate the residuals of the FNMA method Res_{FNMA} by subtracting the summed modes (equation 2.4) from the directly calculated Love number ($h_n(s)$).

4: Apply the pure collocation method with the Res_{FNMA} and ~ 16 evenly spaced inverse decay times (in log(s) space) through equation 2.15 to find a set of response values that fits the FNMA residuals.

$$Res_{FNMA}(s) = \sum_{j=1}^{N} \frac{r_j}{s + s_j} \tag{2.15}$$

5: Add the modes and amplitudes of the FNMA (step 2) to the inverse decay times and corresponding response of the pure collocation method determined from step 4.

By combining the two methods, FNMA finds as many of the large physically based modes as possible, while the pure collocation method fits the residual series. If the FNMA is able to find the majority of the major modes, then the FNMA residuals will be smaller and the pure collocation method will have less influence on the final results. If the FNMA misses large modes owing to singularities or because the search domain along the negative s-axis was truncated and is therefore missing a substantial component of the response, then the pure collocation method will supply the missing response. The hybrid method is therefore as robust as the pure collocation method while retaining as many of the physically-based normal modes and amplitudes as possible.

2.5 Results

A comparison of the proposed hybrid method to the three previously described methods for two viscosity profiles, VM5a (Peltier et al., 2015) and S1, is shown in figure 2.3. Viscosity profile S1 was chosen from 500 randomly generated viscosity profiles to have significant modal response for values of s that cause one or more viscoelastic parameters to be singular at some radius r, thus generating numerical issues for the FNMA method and providing a good test of the hybrid method. S1 is similar to VM5a but has a lower viscosity between 100-670 km and higher viscosity between 670 km and the core-mantle boundary.

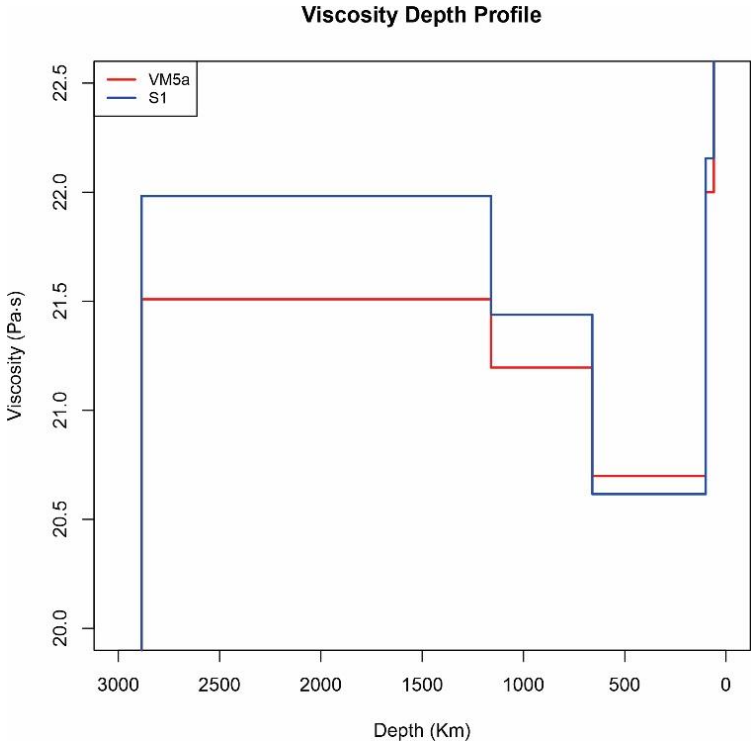

Figure 2.3: Viscosity-depth profiles in a log scale for VM5a (Peltier et al., 2015) and S1.

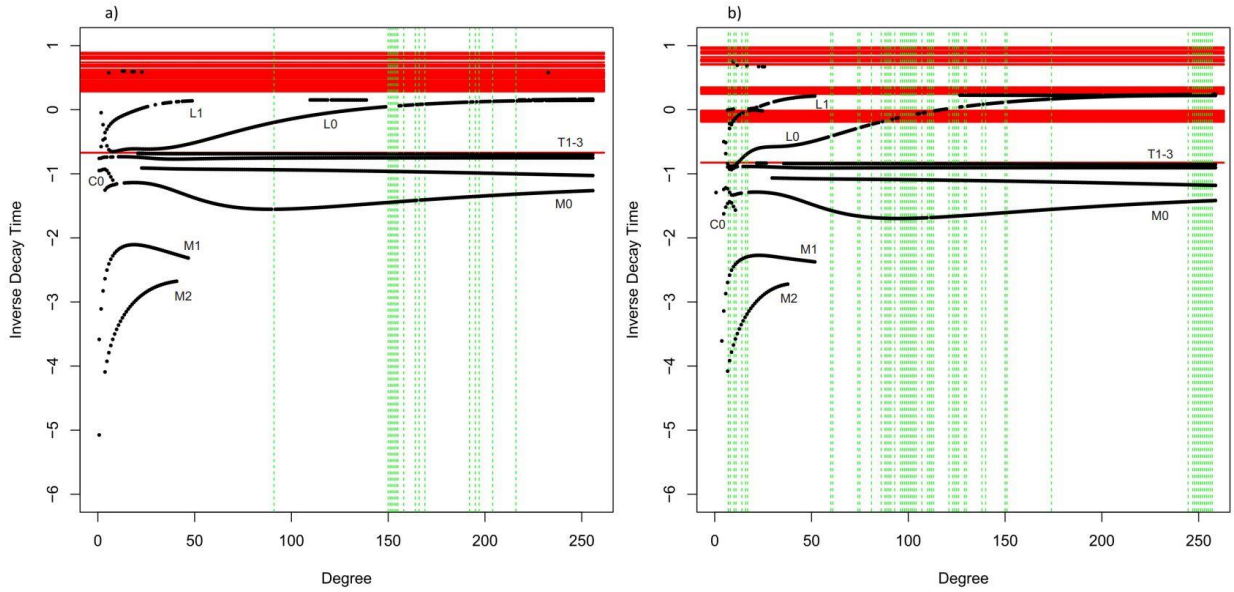

Figure 2.4: Inverse decay time plots for (a) VM5a and (b) S1.The solid red bars, termed singularity zones here, indicate values of s for which one or more of the viscoelastic parameters has a singularity at some radius r. The vertical green lines indicate the spherical harmonic degrees where more then 5% of the response was missing from the FNMA. The modes are labeled based on comparisons to other models (Peltier, 1976; James, 1991).

For VM5a, the major modes do not encroach on the singularity zone, which is the range of s for which one or more of the viscoelastic parameters become singular at some radius r (Figure 2.4a). In contrast, for S1, the L0 and L1 modes are located in one of the singularity zones for a significant range of spherical harmonic degrees (Figure 2.4b). For degrees in which a mode is located in a singularity zone, it is more likely that the mode will not be found using the FNMA method and the modal response will be lacking. For both viscosity profiles, most modes do not intercept the singularity zones, including the M0 mode which carries a significant percentage of the modal response at higher degrees (Wu and Peltier, 1982; James, 1991). Consequently, most of the modal response can be found via FNMA, but for S1, there are degrees where a substantial amount of the modal response is lacking.

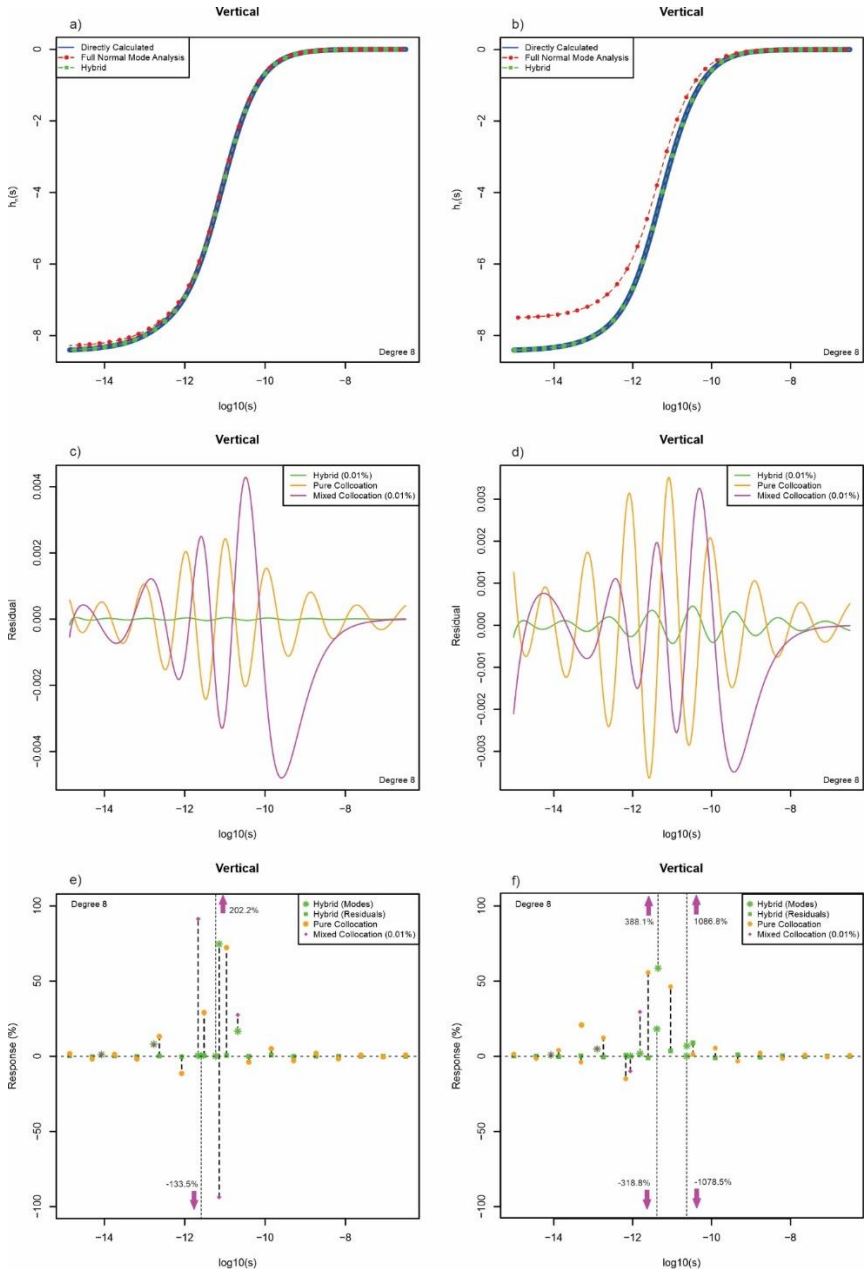

Figure 2.5: Comparison of the hybrid method to FNMA, pure collocation, and mixed collocation methods for spherical harmonic degree 8. Results are given for viscosity structures VM5a (Left column – a, c, and e) and S1 (Right column – b ,d, and f). (a) and (b) Comparison of the directly calculated Love number $h_n(s)$ with the calculated vertical response of both the FNMA and hybrid method. The pure and mixed collocation methods (not shown) agree well with the directly calculated Love numbers for both VM5a and S1, similar to figure 2.1a, and are not displayed for clarity of the figure. (c) and (d) Residuals of the hybrid method, pure collocation, and mixed collocation methods. The FNMA residuals are not shown as the values are too large for the scale. (e) and (f) The modal amplitudes, expressed as a percentage of the infinite-time viscoelastic response, are provided for each method. The vertical black lines show when either the mixed collocation and the hybrid method or the pure collocation and the hybrid method share the same inverse decay time. The FNMA (Hybrid(modes)) and collocation (Hybrid(residuals)) components of the hybrid method are indicated in panels e and f.

Table 2.1: Preferred Method[1] for the VM5a and S1 Viscosity Structures

Method	VM5a			S1		
	Vertical (/256)	Horizontal (/256)	Gravitational[2] (/255)	Vertical (/256)	Horizontal (/256)	Gravitational[2] (/255)
FNMA	0	0	0	0	0	0
Hybrid Method	252	254	251	253	247	249
Pure Collocation	2	1	2	2	5	2
Mixed Collocation	2	1	2	1	4	4

[1]number of spherical harmonic degrees with the smallest RMS residual, where the residual is the difference between the directly calculated Love number $h_n(s)$, $l_n(s)$, or $k_n(s)$ and the Love number constructed from the responses determined by the method. Comparisons were carried out for spherical harmonic degrees 1 to 256.

[2]The degree-1 gravitational response is nil in a centre-of-mass system and counting ranged from degrees 2 to 256

A comparison of the hybrid method to the other methods is provided in figure 2.5 for the viscosity profiles VM5a and S1. At spherical harmonic degree 8, the Hybrid method is able to match the directly calculated Love numbers extremely well, similar to the collocation methods, for both VM5a and S1 (Figure 2.5a and 2.5b). The Hybrid method also has the smallest residuals (Figure 2.5c and 2.5d). It has a number of responses with negative amplitudes, which is thought to be unrealistic, but their amplitudes are smaller than what was found by both the pure and mixed collocation methods (Figure 2.5e and 2.5f). The Hybrid method is favoured for most spherical harmonic degrees regarding the fit to the directly calculated Love numbers (Table 2.1).

2.6 Discussion

With the S1 viscosity profile, the FNMA method has significant deviation from the directly calculated Love numbers (Figure 2.5b) for this spherical harmonic degree (degree 8), signifying a significant missing modal response. Nevertheless, the hybrid method agrees best with the directly calculated Love numbers, indicated by it having the smallest residuals (Figure 2.5d), even though there is a significant missing modal response. Comparing the hybrid results between VM5a and S1, the residuals

are much smaller for VM5a (Figure 2.5c). The FNMA method delivers a larger proportion of the Earth model response for VM5a than for S1, leaving the collocation component of the hybrid method with a smaller residual to explain, and this probably explains the relative difference in the size of the residuals.

For both VM5a and S1, the hybrid method has an inverse decay time structure that includes physically based modes and is thus more realistic than either of the collocation methods. The hybrid method has less prominent negative vertical responses then the pure collocation method while also not having the extreme values (exceeding ±100%) that the mixed collocation method has. The hybrid method does produce larger negative amplitudes for S1 than for VM5a, probably because the collocation component of the hybrid method is explaining a larger fraction of the total response.

The mixed collocation method can fail in an extreme way that the hybrid method can avoid (Figure 2.5f). For two inverse decay times, the response amplitudes given by the mixed collocation component exceed ±ten times the total viscoelastic response. The mixed method uses the inverse decay times found from the FNMA, and if the normal modes are too close to one another, then the mixed collocation method can experience an ill-conditioned least-squares solution.

The hybrid method was applied to models A and B of Mitrovica and Peltier (1992) to further compare the methods (Figure 2.6). Model A has a lower-mantle viscosity of $2x10^{21}$ Pa s and upper-mantle viscosity of 10^{21} Pa s, while Model B has a larger lower-mantle viscosity ($5x10^{21}$) and smaller upper-mantle viscosity ($5x10^{20}$). The hybrid method is able to improve the fit compared to the pure and collocation methods. The hybrid method, like all of the other methods, matches the directly calculated Love numbers extremely well (Figure 2.6a and 2.6b), but through the residuals (Figure 2.6c and 2.6d), one can see that the hybrid method results in the smallest residuals. The hybrid method also produces the most realistic modal amplitudes. Unlike VM5a and S1 (Figure 2.5), Models A and B are examples where the mixed collocation method does not have numerical issues. The mixed collocation method

does well at calculating the response amplitudes that generally compare well to FNMA amplitudes, but for both Model A and B there are two points where the mixed collocation amplitudes overshoots and undershoots the FNMA amplitudes.

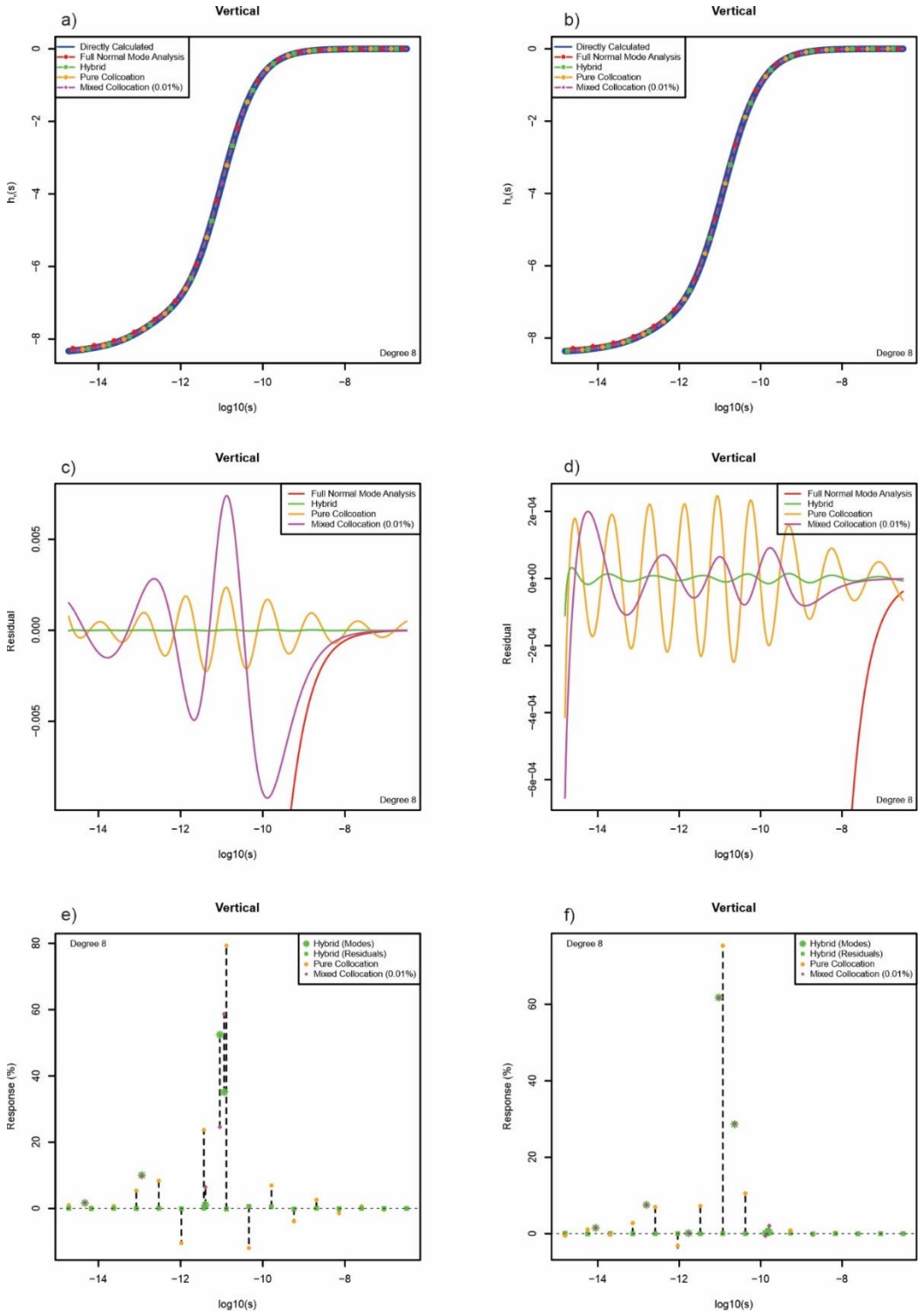

Figure 2.6: Similar to figure 2.5, but for Earth models A and B (see text). (a) and (b) Comparison of the directly calculated Love number $h_n(s)$. (c) and (d) Residuals of the hybrid method, pure collocation, and mixed collocation methods. (e) and (f) The modal amplitudes, expressed as a percentage of the infinite-time viscoelastic response, are provided for each method. The vertical black lines show when two of the methods share the same inverse decay time.

One point of interest regarding the comparison between the pure collocation method and the hybrid method is the number of points that each method fits. The hybrid method as described will always have more points than the pure collocation method, assuming the same number of points are used for the pure collocation method for both FNMA residuals in the hybrid method and the directly calculated values for the pure collocation method, which one could argue is the reason why the hybrid method performs better. Figure 2.7 shows a comparison of the hybrid method and the pure collocation method where the two methods are forced to have the same number of inverse decay times.

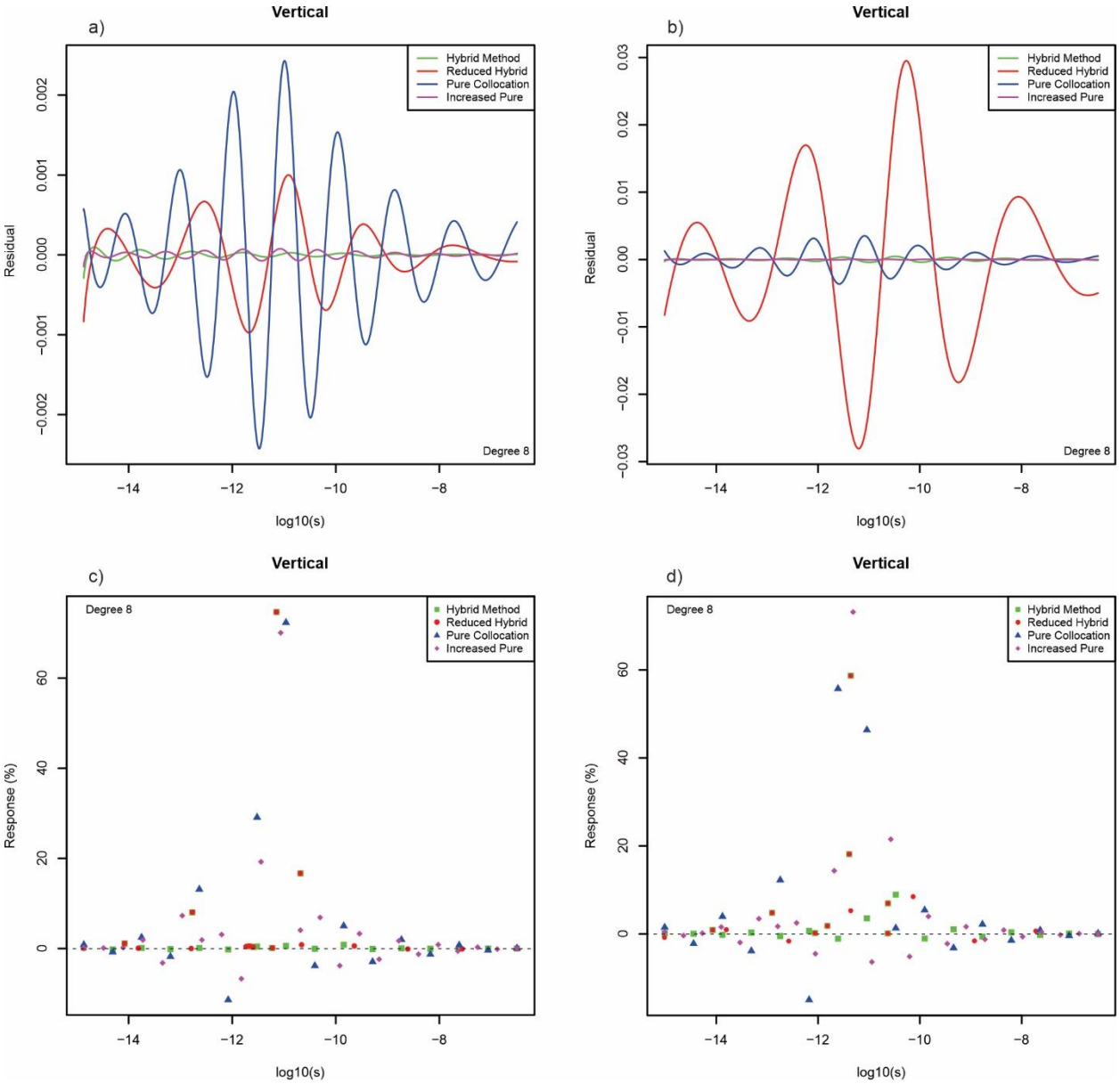

Figure 2.7: Comparison of the hybrid method and the pure collocation method for spherical harmonic degree 8 while forcing the methods to share the same number of inverse decay times. The 'hybrid' method and the 'pure collocation' method are the original methods while the 'reduced hybrid' refers to limiting the number of inverse decay times added to match the original pure collocation method and the 'increased pure' method refers to increasing the number of inverse decay times used to match the original hybrid method. Results are given for viscosity structures VM5a (Left column – a and c) and S1 (Right column – b and d). (a) and (b) are the residuals while (c) and (d) are the modal amplitudes expressed as a percentage of the infinite-time viscoelastic response.

With VM5a, the hybrid method does better then the pure collocation method in both instances regarding the residuals. However, with S1 the reduced hybrid does a worse job at matching the directly calculated Love numbers then just the pure collocation method. This is because the FNMA method does

not collect all of the major normal modes. With a smaller number of inverse decay times to work with and a more significant portion of the modal response to fit, the pure collocation part of the hybrid method is not able to match the directly calculated Love numbers as well. When the number of inverse decay times are the same between the methods, the residuals are much more comparable in amplitude. In both VM5a and S1 the hybrid method is producing smaller negative vertical response amplitudes than the pure collocation method regardless of the number of inverse decay times used. The pure collocation method still generates large negative amplitudes, while the hybrid method provides a more realistic modal structure, even though the residuals are of similar magnitude.

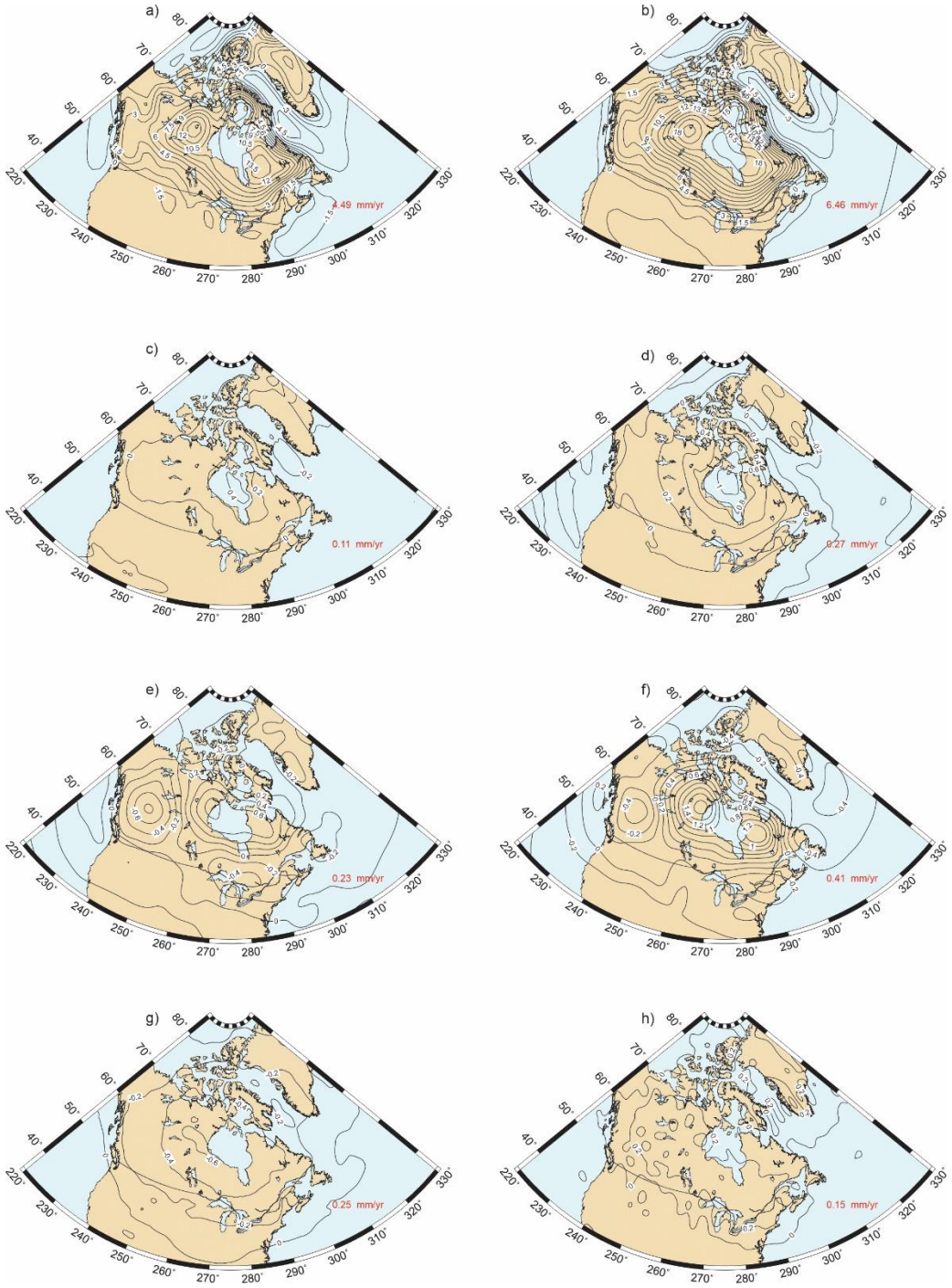

Figure 2.8: Predicted uplift rates in North America using the ICE6G_C ice load (Peltier et al., 2015). Results are given for viscosity structures VM5a (Left column – a, c, e, and g) and S1 (Right column – b, d, f, and h). (a) and (b) are predicted uplift rates generated using the hybrid method. The differences in predicted uplift are given between the hybrid method and (c and d) FNMA, (e and f) pure collocation, and (g and h) mixed collocation. The values on the bottom right of each map represents the RMS of (a and b) uplift rates and (c through h) differences in uplift rates within the displayed region.

Table 2.2: Largest Differences in Computed Vertical Uplift Rate for Different Methods Compared to the Hybrid Method

Method compared to Hybrid	VM5a						S1					
	Difference[1]			Ratio[2]			Difference[1]			Ratio[2]		
	Value (mm/yr)	Lat	Long	Value (%)	Lat	Long	Value (mm/yr)	Lat	Long	Value (%)	Lat	Long
FNMA	0.425	57	280	13.6	73	238	1.112	61	276	19.5	73	288
Pure Collocation	0.869	63	266	35.4	61	236	1.647	63	264	46.7	71	334
Mixed Collocation	0.634	61	256	26.5	51	258	0.467	55	244	29.3	65	322

[1]The difference between the hybrid method vertical response and the vertical response of the other methods. The largest values are shown with the respective coordinates.

[2]The percent difference of the vertical response between the hybrid method and the other methods relative to the hybrid method. The percentage difference is taken in regard to each value at all coordinate points.

The comparison of the predicted uplift rates for the VM5a and S1 Earth models (Figure 2.8) reveals significant differences between the methods. Despite the relatively small differences in the residuals in figure 2.5c and 2.5d, the predicted uplift rates vary significantly. The first comparison to highlight is the difference between the FNMA and the hybrid method for VM5a and S1 in figures 2.8c and 2.8d. For VM5a, the differences are relatively small (RMS difference of 0.11 mm/yr, peak difference 0.43 mm/yr in the centre of Hudson Bay (Table 2.2)) while S1 has a larger difference (RMS difference of 0.27 mm/yr, peak difference of 1.11 mm/yr in the centre of Hudson Bay). This is not unexpected as the FNMA does not find important modes for many spherical harmonic degrees for S1 (Figure 2.4b).

For the comparison with the pure collocation method (Figure 2.8e and 2.8f), the differences are more localized to specific regions. This would suggest that the difference in the methods is more prominent at higher spherical harmonic degrees. This is contrasted by the difference plots for the mixed collocation method in figure 2.8g and 2.8h. The difference here is much broader and covers the majority of the displayed region. This would indicate that the difference between the two methods is more prominent for smaller spherical harmonic degrees.

At high spherical harmonic degree, the modal response is dominated by a single mode. The pure collocation method, with a number of uniformly spaced inverse decay times, distributes the response amongst the inverse decay times closest to the modal decay time, and may give rise to differences at high spherical harmonic degree, which corresponds to shorter spatial wavelength. Conversely, the mixed collocation method, fitting the response to the modal decay times, fits the single mode relatively well at high spherical harmonic degree, but distributes the response among the number of physical modes at low spherical harmonic degree, leading to differences that are longer-wavelength.

Table 2.2 shows that the differences in the uplift rates are as large as 1.647 mm/yr, and expressed as a ratio in the uplift rates, can be as high as 47%, for the pure collocation method compared to the hybrid method. These differences are significant, both absolutely and relatively. For FNMA, the difference ratio is not as high, peaking around 13% to 19%, while the pure collocation method has a much higher difference ratio, peaking around 35% to 47%. Given that all the methods have residuals that are small relative to the directly calculated values, the significant difference in the uplifts between the methods is likely caused by the differences in the structure of the inverse decay times and the corresponding response amplitudes. The pure collocation method generates consistent inverse decay times with negative amplitudes while the mixed collocation method can potentially generate responses with extreme values for the amplitudes. In contrast, the hybrid method retains a generally realistic modal structure (like the FNMA) while also generating the smallest residuals.

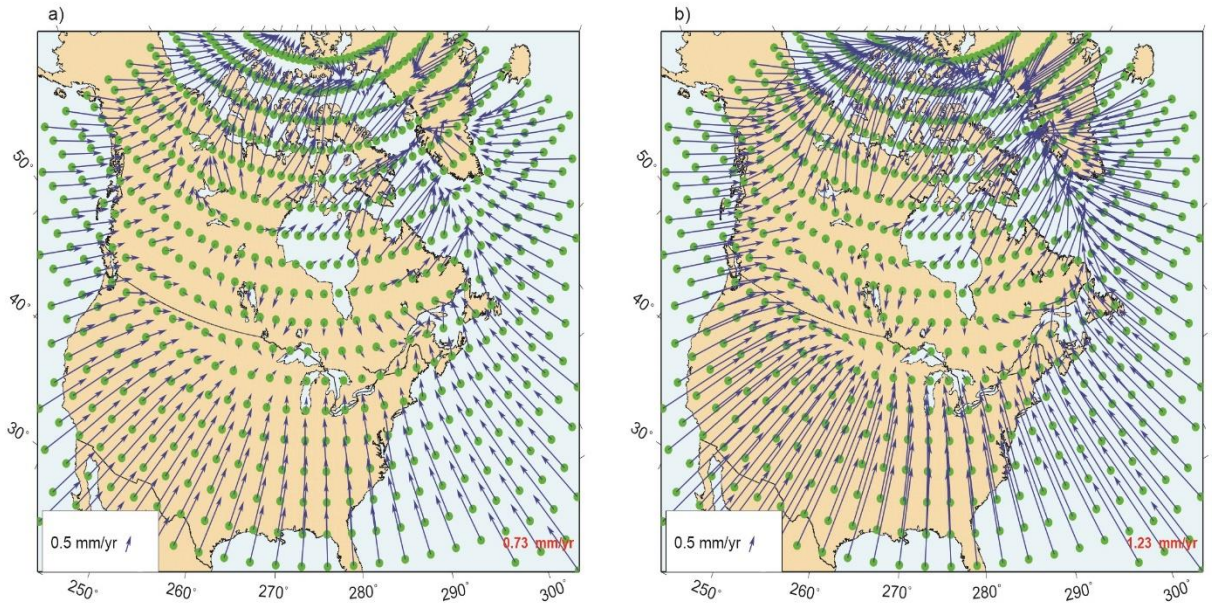

Figure 2.9: Predicted horizontal crustal motion of North America using the ICE6G_C ice load (Peltier et al., 2015) and the hybrid method. This viscosity profile is VM5a for (a) and is S1 for (b). The value on the bottom right of both maps represents the RMS of the motions shown on the map.

Table 2.3: RMS Values of the Difference in Horizontal Motions Compared to the Hybrid Method for Different Methods.

Method compared to Hybrid	VM5a	S1
	RMS (mm/yr)	RMS (mm/yr)
-	0.73	1.23
FNMA	0.02	0.31
Pure Collocation	0.09	0.10
Mixed Collocation	0.14	0.30

Table 2.4: Largest Differences in Computed Horizontal Motions for Different Methods Compared to the Hybrid Method.

Method compared to Hybrid	VM5a						S1					
	Difference[1]			Ratio[2]			Difference[1]			Ratio[2]		
	Value (mm/yr)	Lat	Long	Value (%)	Lat	Long	Value (mm/yr)	Lat	Long	Value (%)	Lat	Long
FNMA	0.077	66	285	4.6	57	300	0.680	63	306	61.7	60	300
Pure Collocation	0.268	63	258	14.7	72	285	0.292	60	255	19.6	54	297
Mixed Collocation	0.307	45	249	21.3	57	300	0.676	36	282	51.0	48	231

[1]The difference between the hybrid method vertical response and the horizontal response of the other methods. The largest values are shown with the respective coordinates.

[2]The percent difference of the horizontal response between the hybrid method and the other methods relative to the hybrid method. The percentage difference is determined with respect to the value at each location.

The horizontal crustal motion is shown in figure 2.9 for the Hybrid method and a comparison with the other methods is given in tables 2.3 (RMS comparison) and 2.4 (peak differences). The horizontal velocities display features similar to the vertical velocities. The differences between the different methods are smaller for VM5a than for S1 (Table 2.3), largely because the FNMA method is able to find more of the modal response for VM5a. The peak differences range from 0.08 to 0.31 mm/yr (VM5a) and 0.29 to 0.68 mm/yr (S1), a significant fraction of the RMS horizontal velocity. The ratios in the horizontal motions reach as high as 62% for S1 between the hybrid method and the FNMA, likely caused by significant missing modes. These differences are significant and further support the finding that a realistic modal structure, including modal amplitudes, is important for crustal motion predictions as Global Navigation Satellite Systems (GNSS) sites monitor both vertical and horizontal crustal motion to less than a millimetre per year (Sella et al., 2007; Kreemer et al., 2018).

2.7 Conclusion

A hybrid method to compute the surface loading response of spherically symmetric Maxwell viscoelastic Earth models is introduced and shown to circumvent some problems that previously described approaches exhibit. Differences in the computed vertical and horizontal crustal velocity between the hybrid method and others considered in this study (free normal mode analysis (FNMA), pure collocation, mixed collocation) were computed and found to be significant. The hybrid method combines the normal modes found via the FNMA with the robustness of the pure collocation method, which is applied to the residuals of the FNMA method. Thus, the hybrid method delivers an Earth model response that includes the true normal modes, albeit with some important modes possibly missing for some spherical harmonic degrees, and an additional set of inverse decay times with amplitudes calculated to provide good agreement with the directly calculated viscoelastic Love number. The hybrid method is robust and flexible and permits exploration of mantle viscosity parameter space without manual intervention. The uplift rates and horizontal motions predicted by the hybrid method have significant differences with previous methods, reaching over 1 mm/yr in vertical and 0.5 mm/yr in horizontal for the VM5a and S1 viscosity model examined here. Thus, the hybrid method may be the preferred solution method for a classical Laplace-transform approach to solving the surface loading problem for compressible Maxwell viscoelastic Earth models.

The hybrid method, which assumes a laterally homogeneous Earth model, complements other numerical approaches that allow the incorporation of lateral heterogeneity and non-linear rheology (Tromp et al., 1999; Martinec, 2000; Latychev et al., 2005b; Wu et al., 2006; Hampel et al., 2019). Thus, it may serve as a reconnaissance tool for discerning regional, or globally averaged, Earth model viscosity parameters, in preparation for the application of other modelling tools that incorporate more realistic elements of Earth structure, such as lateral heterogeneity or non-linear rheology.

Chapter 3: Exploration of Earth Model Parameter Space: Effect of Lithosphere Thickness and Radial Mantle Viscosity Profile for Vertical and Horizontal Crustal Motions in North America

3.1 Introduction

Glacial Isostatic Adjustment (GIA) is a process where the Earth's surface undergoes displacement from glacial expansion and retreat. Changes to the surface loading from ice sheet fluctuations induce not only elastic response but also viscous flow in the Earth's mantle and corresponding crustal displacements at the surface that can be measured and observed. GIA-induced crustal motions from the Last Glacial Maximum (LGM) generate present-day crustal motions across the globe, with large rates observed in North America, Greenland, Fennoscandia, and Antarctica (Peltier, 1986; James and Ivins, 1998; Simon et al., 2016). GIA affects other geophysical phenomena including relative sea-level changes (Coulson et al., 2021), gravitational changes (Lombard et al, 2007; Cazenave et al., 2009), and earthquake activity (Steffen et al 2014; Ojo et al., 2021). The broad influence of GIA across a range of geophysical observables motivates development of models to predict these responses.

GIA models are composed of two components, a surface loading model and an Earth response model. The surface loading model represents the growth and decay of the ice masses and the ocean loading effect (Woodward, 1888; Mitrovica and Peltier, 1991a; Mitrovica and Milne, 2003). The Earth model specifies how the Earth responds to the changing surface load. The Earth models used in this study are spherically symmetric and possess seismically constrained density and elastic-parameter structure with a linear Maxwell rheology (Peltier, 1974; Wu and Peltier, 1982; Mitrovica and Peltier,

1992). Viscosity of the Earth's mantle varies radially and is typically specified for a small number of layers.

This chapter focuses on varying Earth model parameters – effective lithospheric thickness and radial mantle viscosity profile – to determine the effect on predicted horizontal and vertical crustal motion in North America. A 3-layer approximation for the mantle viscosity profile is assumed, and responses are computed using the hybrid normal mode-collocation method described in Chapter 2. This allows Earth model responses to be generated quickly and thus a more complete examination of the parameter space can be undertaken. The predictions are compared to Global Navigation Satellite System (GNSS) observations of vertical and horizontal crustal motion to find best-fitting Earth models.

This chapter is structured by first introducing the observational data set. This is followed by an explanation of how the Earth model parameters were chosen and responses (vertical and horizontal crustal motion) computed. A goodness-of-fit statistic is used to measure how well the predictions of a particular Earth model agree with the observations. The results are compiled and presented with a discussion on the overall effects of the changing parameters. The best fitting models are determined and compared to previous inferences for North America.

3.2 Observational Dataset

The observational dataset was downloaded from the Nevada Geodetic Laboratory repository of MIDAS GNSS velocity fields (Blewitt et al., 2018, http://geodesy.unr.edu/) (Figure 3.1). The dataset was provided in the IGS14 reference frame (Kreemer et al., 2014) and was downloaded on August 9th, 2022. A no-net-rotation reference frame was found by defining and removing an Euler pole of rotation (Kreemer et al., 2014) for the horizontal motions using around 30 sites in central and eastern United States. The horizontal crustal motions show a consistent westward motion in the IGS14 reference frame (Figure 3.1a). In the no-net-rotation reference frame defined by the 30 sites, the horizontal motions for

most of Canada and the northern United States point southward while sites around the central United States point in a more or less random directions (Figure 3.1b). The maps show uplift across most of Canada with the largest uplift rates being centralized near Hudson Bay with subsidence across most of the United States and most of the Canada-United States border (Figure 3.1c).

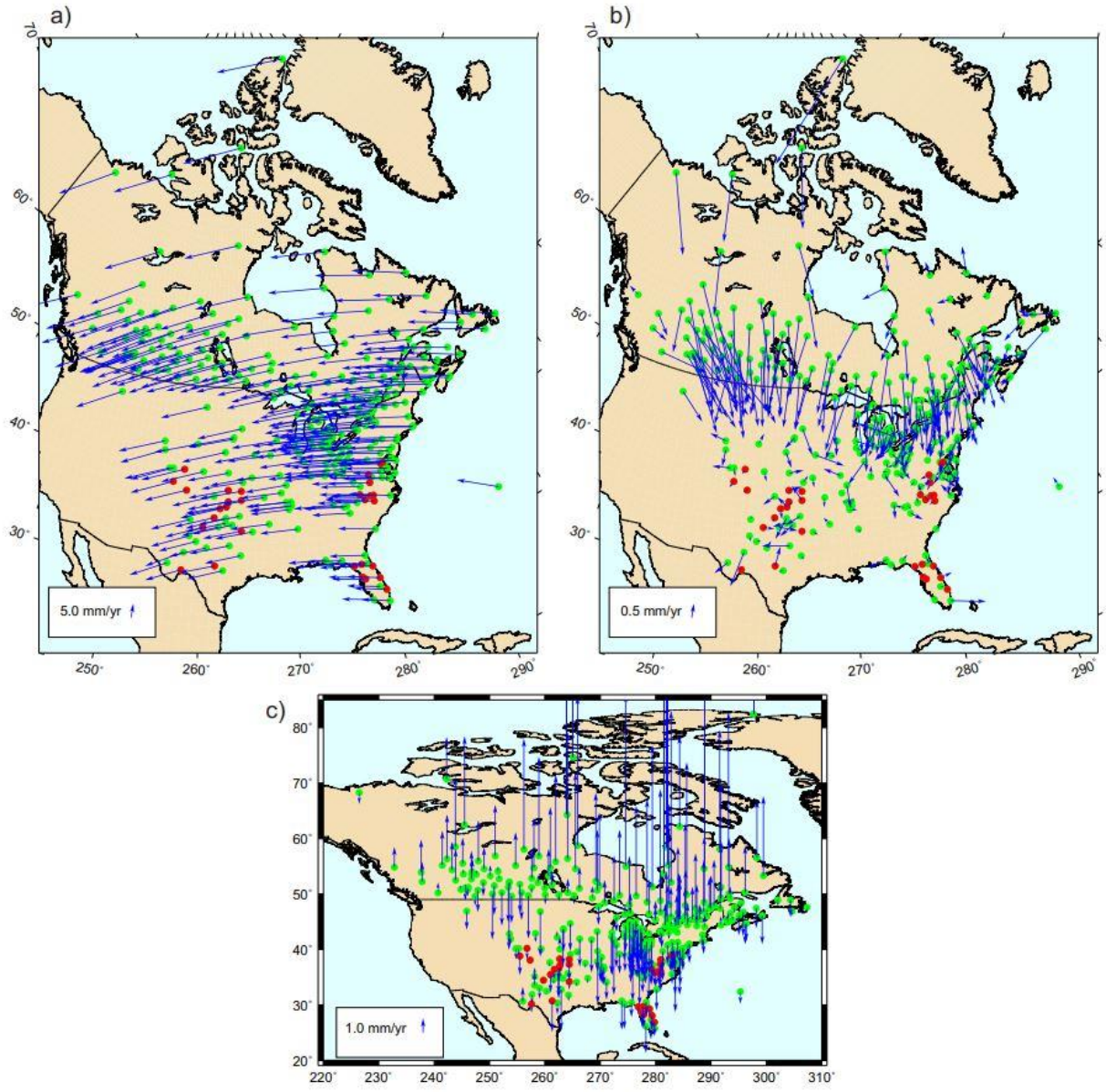

Figure 3.1: Maps of the IGS14 horizontal and vertical observational GNSS data. (a) Horizontal motions downloaded from the Nevada Geodetic Laboratory (Blewitt et al., 2018, http://geodesy.unr.edu/), b) the same horizontal motions after defining a no-net-rotation reference frame. c) The vertical motions. The red dots indicate the sites that were used to define the no-net-rotation reference frame.

The GNSS sites used for the horizontal and vertical crustal motions have been collecting crustal motion data for at least 4 years to ensure sufficiently long GNSS time series. GNSS sites were chosen to be located in eastern and central North America, avoiding sites in tectonically active western North America. There are many geophysical phenomena aside from GIA that produce a notable effect on crustal motion in North America which would be captured by these GNSS sites. Some examples are the effects of ground water from changing water volume of the great lakes (Argus et al., 2020; Wang et al., 2022) and the recent loading changes caused by the melting of glaciers, ice caps, and ice sheets in the Canadian arctic archipelago and Greenland (Riva et al., 2017; Coulson et al., 2021). These processes, among others are not considered in this study.

3.3 Method

In order to explore Earth rheology parameters and determine best-fitting values for the Earth models, 8 lithosphere thicknesses were tested in conjunction with randomly generated viscosity profiles. The ranges for the parameters are shown in table 3.1.

Table 3.1: Viscoelastic Earth Response Model Parameter Ranges.

Lithospheric Thicknesses (km)	Asthenosphere/Upper Mantle Viscosity Range (Pa·s)	Transition Zone Viscosity Range (Pa·s)	Lower Mantle Viscosity Range (Pa·s)
40, 60, 80, 100, 120, 180, 240, 300	$1.00 \times 10^{20} – 1.58 \times 10^{21}$	$3.16 \times 10^{20} – 2.00 \times 10^{22}$	$7.94 \times 10^{20} – 6.31 \times 10^{22}$

The boundaries of the viscous layers are at depths of 420 km, 670 km, and the core-mantle boundary at 2885.5 km. With these parameter ranges, 500 random viscosity profiles were generated. The only logic implemented in the random viscosity profile generation ensured that the lower mantle viscosity was greater than or equal to the transition zone viscosity, and the transition zone viscosity was greater than or equal to the asthenosphere/upper mantle viscosity. This was implemented to ensure that viscosity

increases with depth. The same 500 random viscosity profiles were used for each lithosphere thickness, which ranged from 40 to 300 km (Table 3.1).

Using these profiles, Earth model responses were generated with the hybrid normal mode-collocation method, as discussed in Chapter 2, up to degree 256. This method combines the full normal mode analysis and the pure collocation method (Mitrovica and Peltier, 1992) and assumes a laterally homogeneous Earth. The hybrid method was chosen as it is a robust method for finding the inverse decay times and amplitudes while maintaining as much of the physically-based modal solution as possible. GIA model predictions of vertical and horizontal crustal motion were generated with the ICE6G_C ice loading history (Argus et al., 2014) and the randomly generated Earth model responses. The ocean loading component is included in the calculations (Kendall et al., 2005; Simon, 2014; Simon et al., 2015, 2016).

Each set of model predictions is then compared to the IGS14 observational data set with both the data set and the predictions in the center of mass reference frame (Kreemer et al., 2014; Blewitt et al., 2018). The comparison was made by finding the root mean square (RMS) difference between the observations and the predictions, with a smaller RMS value indicating a better fit. For vertical crustal motions, this is simply a direct comparison. For horizontal crustal motions, the observational data set and the GIA model predictions are placed in the same reference frame. An Euler pole of rotation was found using a number of GNSS sites in the central United States for each model prediction, and compared to the observations, which are also placed in a no-net-rotation frame using the same sites as described in section 3.2 above (Kreemer et al., 2014; Blewitt et al., 2018).

Best fits (minimum RMS values) to the observations were found for the vertical, horizontal, and combined vertical and horizontal crustal motion observations. For the combination, the following relation was employed

$$RMS_C = \sqrt{\frac{RMS_H^2 + (c * RMS_V)^2}{2}} \quad (1)$$

where RMS_C, RMS_H, and RMS_V, are the RMS difference value for the combined, horizontal, and vertical respectively. The value c refers to the ratio

$$c = \frac{RMS_{HMax} - RMS_{HMin}}{RMS_{VMax} - RMS_{VMin}} \quad (2)$$

where the max and min refer to the largest and smallest RMS difference value of both the horizontal, H, and vertical, V, for the given lithosphere thickness. This ratio is incorporated into the combined RMS calculation to ensure that the magnitude of the vertical and horizontal RMS values are similar. This weighting prevents a bias toward minimizing one component over the other due to the magnitude of the respective RMS values.

3.4 Results

For a baseline example, consider the results for the VM1 viscosity profile (Peltier et al., 1976) (1 x 10^{21} Pa·s asthenosphere/upper mantle, 1 x 10^{21} Pa·s transition zone, 2 x 10^{21} Pa·s lower mantle) for horizontal (Figure 3.2) and vertical velocities (Figure 3.3) (Peltier et al., 1976).

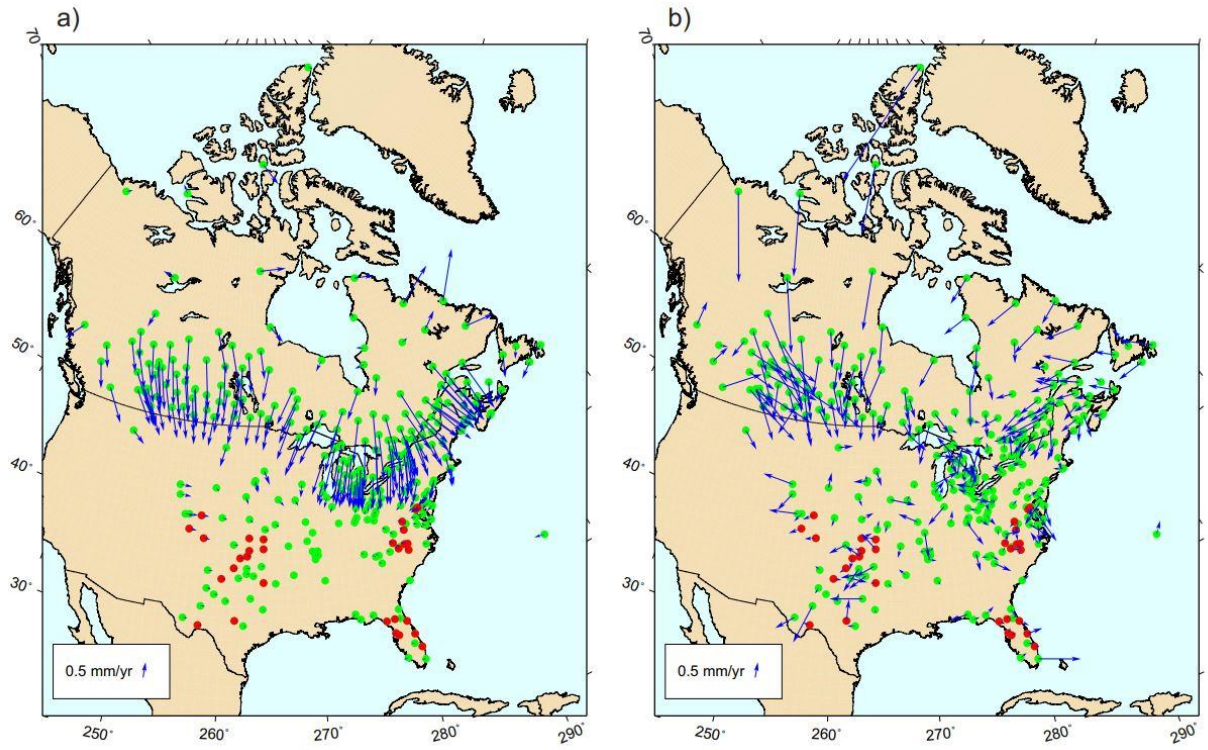

Figure 3.2: Horizontal motions for the VM1 viscosity profile (Peltier et al., 1976) using the ICE6G_C surface loading model (Argus Et al., 2014). a) predicted motion in the no-net-rotation reference frame, b) residual velocities generated from the IGS14 observational dataset.

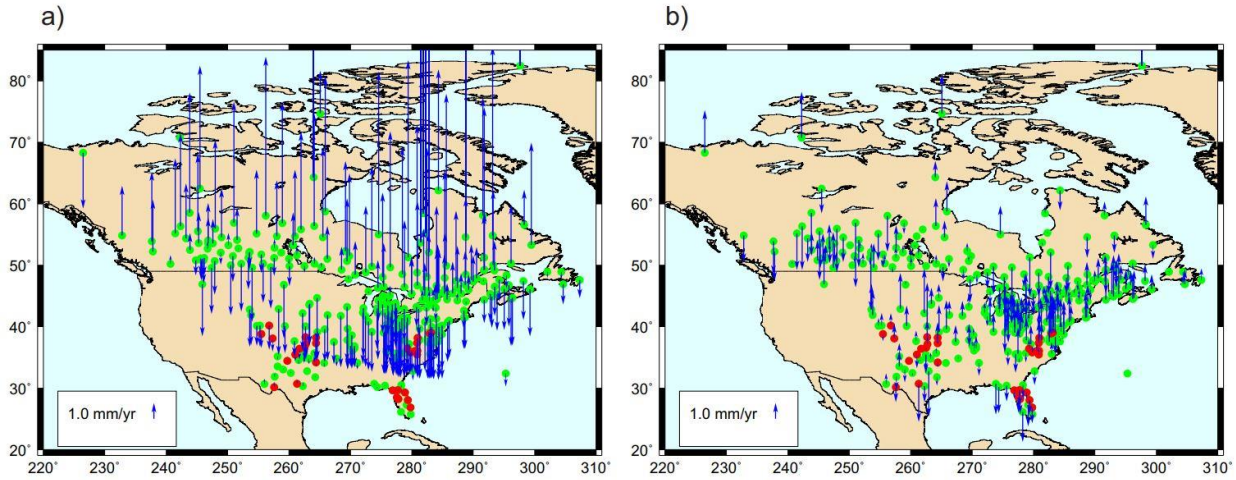

Figure 3.3: Vertical motions for the VM1 viscosity profile (Peltier et al., 1976) using the ICE6G_C surface loading model (Argus et al., 2014). Map a) shows the predicted motion while map b) shows the residuals generated from the IGS14 observational dataset.

With the horizontal motions, VM1 has some trouble matching the observed values. A number of sites

near the United States-Canada border have residuals that all point southward at varying magnitudes

while most of the sites centred in the United States have residuals directed away from the centre. This consistent residual pattern indicates that a large portion of the horizontal response is not being explained with VM1, though an interpretation is difficult due to the change to the no-net rotation reference frame for both the observational dataset and the VM1 model. VM1 does give a relatively accurate response for the vertical crustal motions. There are non-zero residuals across all sites, with the largest residuals being around the Great Lakes, likely due to a large hydrological signal (e.g., Argus et al., 2020; Wang et al., 2022), but the overall residuals are small compared to the predicted crustal motions.

For a quantitative comparison, one can compare the results of VM1 to a null model. A null model in this context refers to a GIA model with no GIA deformation. The RMS taken from the null model (Table 3.2) will just be the RMS of the observational data set, thus comparing VM1 (Table 3.3) to the null model will show by how much the model improves the comparison.

Table 3.2: RMS difference values for the null model.

Horizontal RMS (mm/yr)	Vertical RMS (mm/yr)	Combined[1] RMS (mm/yr)
1.321	3.244	1.423

[1]The weighting function was determined by using the range of vertical and horizontal RMS values generated from the 500 random viscosity profiles for the 120 km thick lithosphere (equations 3.1 and 3.2).

Table 3.3: RMS difference values for VM1.

Horizontal RMS (mm/yr)	Vertical RMS (mm/yr)	Combined[1] RMS (mm/yr)
0.834	1.297	0.670

[1]The weighting function was determined by using the range of vertical and horizontal RMS values generated from the 500 random viscosity profiles for the 120 km thick lithosphere (equations 3.1 and 3.2).

A significant amount of the crustal response is explained with VM1 when compared to a null model. VM1 does a fairly decent job at modeling the vertical crustal motions, improving the fit by 60% over the null model, while the horizontal crustal motions are improved, but only by around 30%. As stated before, the residuals for the vertical motions are relatively small across most of Canada and parts

of the United States with the largest around the Great Lakes, while the horizontal residuals are not as well explained as a large number of sites across southern Canada show large residuals all pointing southward. This comparison indicates that VM1 does a decent job explaining the majority of the vertical crustal response observed, but the model struggles to explain much of the horizontal crustal response.

With a baseline example presented, the 500 random viscosity profiles were generated for each lithosphere thickness. Earth model response files were generated, and horizontal and vertical crustal motions were computed and compared to the observations through the RMS calculation described above. These results are represented by 3D scatter plots, shown in figure 3.4, for the 100 km thick lithosphere case.

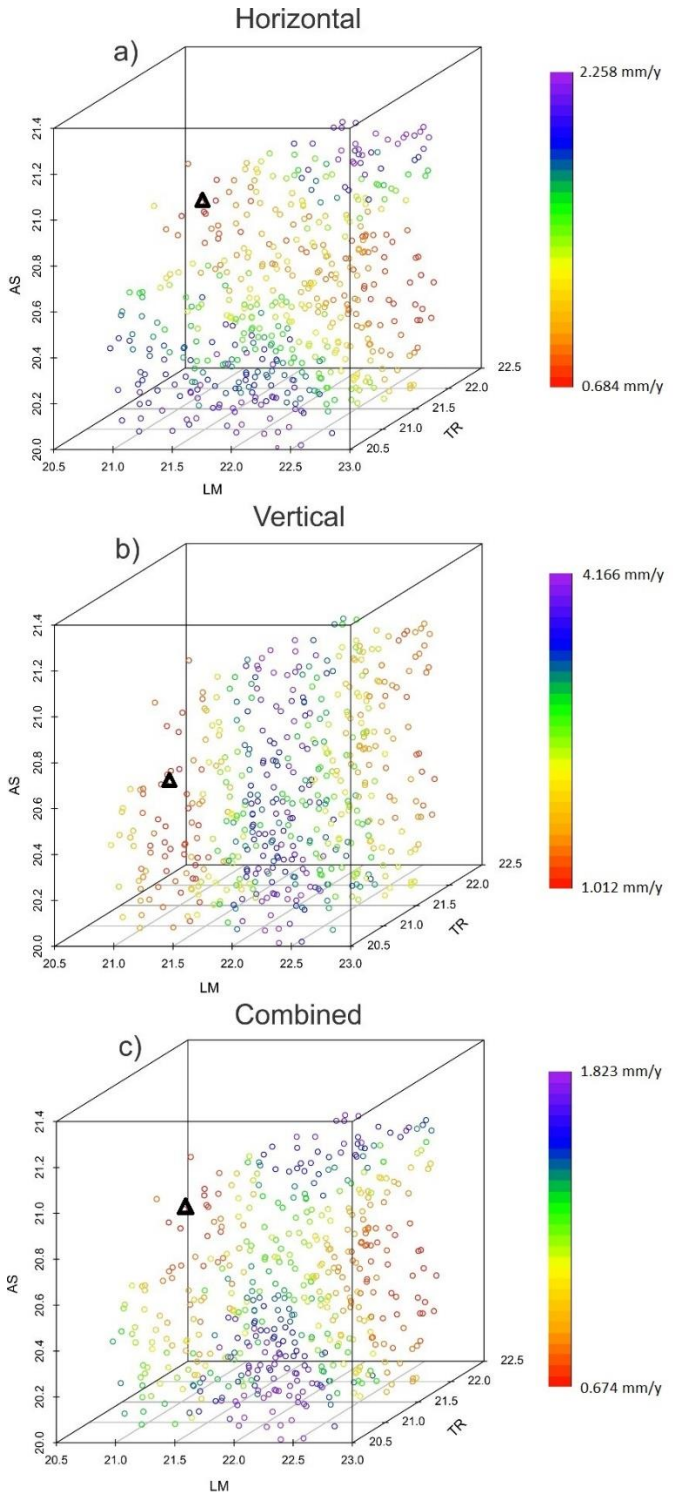

Figure 3.4: 3D scatter plots showing the RMS values for the 500 different viscosity profiles, assuming a 100 km thick lithosphere. Warmer colours refer to smaller RMS while the colder colours refer To larger RMS. a) horizontal RMS, b) vertical RMS, c) combined RMS. The black triangle in each panel is the smallest RMS for this lithospheric thickness. AS is the asthenosphere/upper mantle, TR is the transition zone, and LM is the lower mantle. Labels are logarithms (base 10) of layer viscosity.

For the horizontal scatter plot (Figure 3.4a), the scatter plot shows two regions of warmer colours. This indicates that there are two local optimal viscosity profiles for this particular lithosphere thickness. This feature is present in the combined scatter plot but is less prominent in the vertical scatter plot. The vertical scatter plot, however, shows another trend, namely the banding of colours on the asthenosphere-transition zone plane. Since the colours are layered in this plane, this indicates that when minimizing the vertical RMS difference, the lower mantle viscosity is the most important factor.

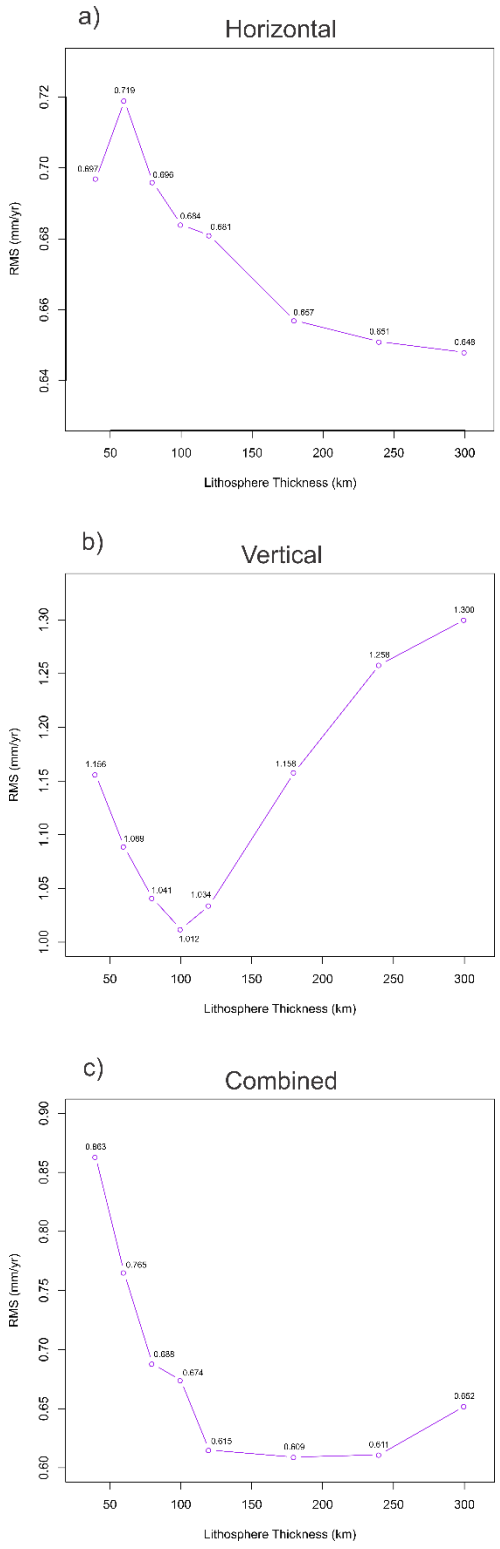

Figure 3.5: Minimum RMS vs lithosphere thickness for a) horizontal motions, b) vertical motions, and c) combined vertical and horizontal motions. Each RMS corresponds to the smallest RMS out of the 500 viscosity profiles tested at the given lithosphere thickness.

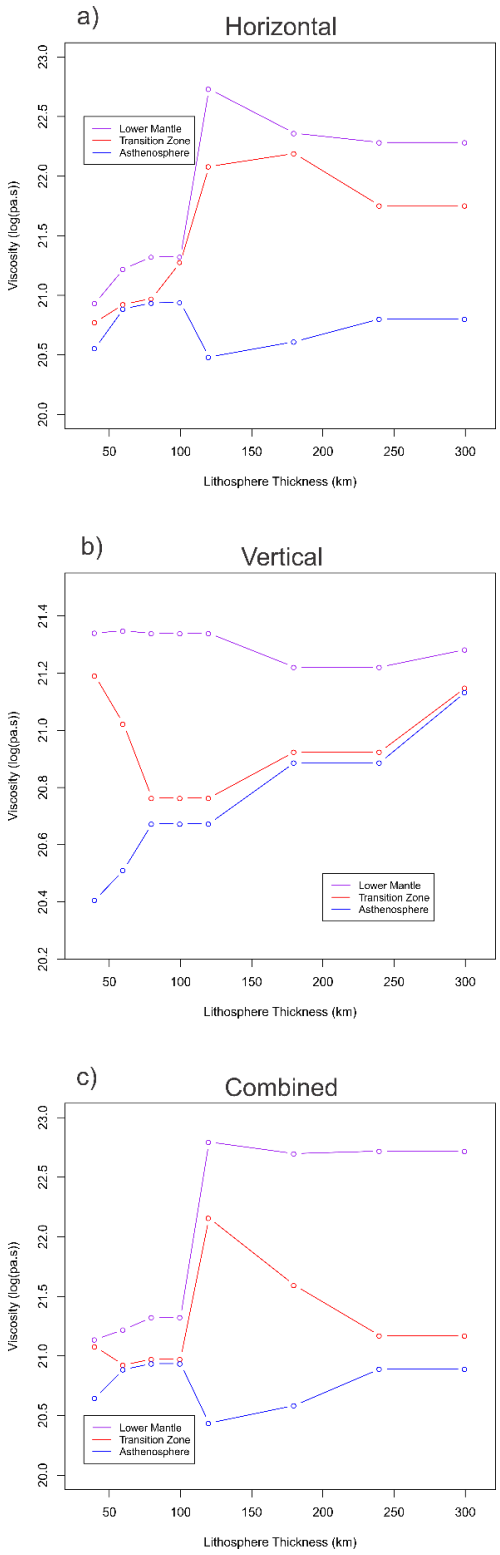

Figure 3.6: Viscosity profile vs lithosphere thickness for a) horizontal motions, b) vertical motions, and c) combined vertical and horizontal motions. Note that the y-axis scale in b) is significantly smaller than a) and c). Each plotted viscosity profile represents the profile that produced the smallest RMS value.

To represent the best models, the smallest RMS for each lithosphere thickness from Figure 3.4 is plotted in Figure 3.5 and the corresponding viscosity profile is plotted in Figure 3.6 as a function of lithosphere thickness. For the horizontal minimization, there is no local or global minimum for the RMS difference as the value continues to decrease as the lithosphere thickness increases (Figure 3.5a). This contrasts to the vertical minimization, which shows a clear global minimum at 100 km (Figure 3.5b). Any lithosphere thickness outside of the 80 – 120 km range comes with a significant increase in the vertical RMS difference. The weighted combination mixes the vertical and horizontal results (Figure 3.5c). There is a range of lithospheric thicknesses for the smallest RMSs, but it is larger than the vertical minimization and ranges from 120 to 240 km.

The optimal viscosity profile is quite different depending on the minimization (Figure 3.6). For horizontal (Figure 3.6a) and combined weighting (Figure 3.6c), there is an abrupt change in the optimal viscosity profile from 100 km to 120 km. The optimal viscosity profiles for lithosphere thickness between 80 and 100 km are similar to that of VM1, but for thicknesses of 120 km and greater, the lower mantle and transition zone viscosity increase by about an order of magnitude, while the asthenosphere viscosity decreases. The vertical minimization (Figure 3.6b) is in contrast to this trend with a relatively consistent viscosity profile across all lithosphere thicknesses. Given that the combined viscosity profile plot shows trends closer to the horizontal viscosity profile, this indicates that the horizontal crustal motions are fit more poorly at optimal vertical viscosity profiles than vertical crustal motions are poorly fit at the optimal horizontal viscosity profiles.

3.5 Discussion

To explore the abrupt change in optimal viscosity profiles, the local optimal viscosity profile before and after the shift were recorded for the thin lithosphere branch and the thick lithosphere branch. The thin lithosphere branch was extended from 100 km to 120 km, and the thick lithosphere

branch was extended from 120 km to 100 km. The local optimal profile was selected by finding the profile that produced the smallest RMS with a lower mantle viscosity greater than 1 x 10^{22} Pa·s for 100 km and a smallest RMS profile with a lower mantle viscosity of less than 1 x 10^{22} Pa·s for 120 km. These local optimal viscosity profiles and the corresponding RMS value plots are shown in figures 3.7 and 3.8 for the horizontal and combined RMS minimizations.

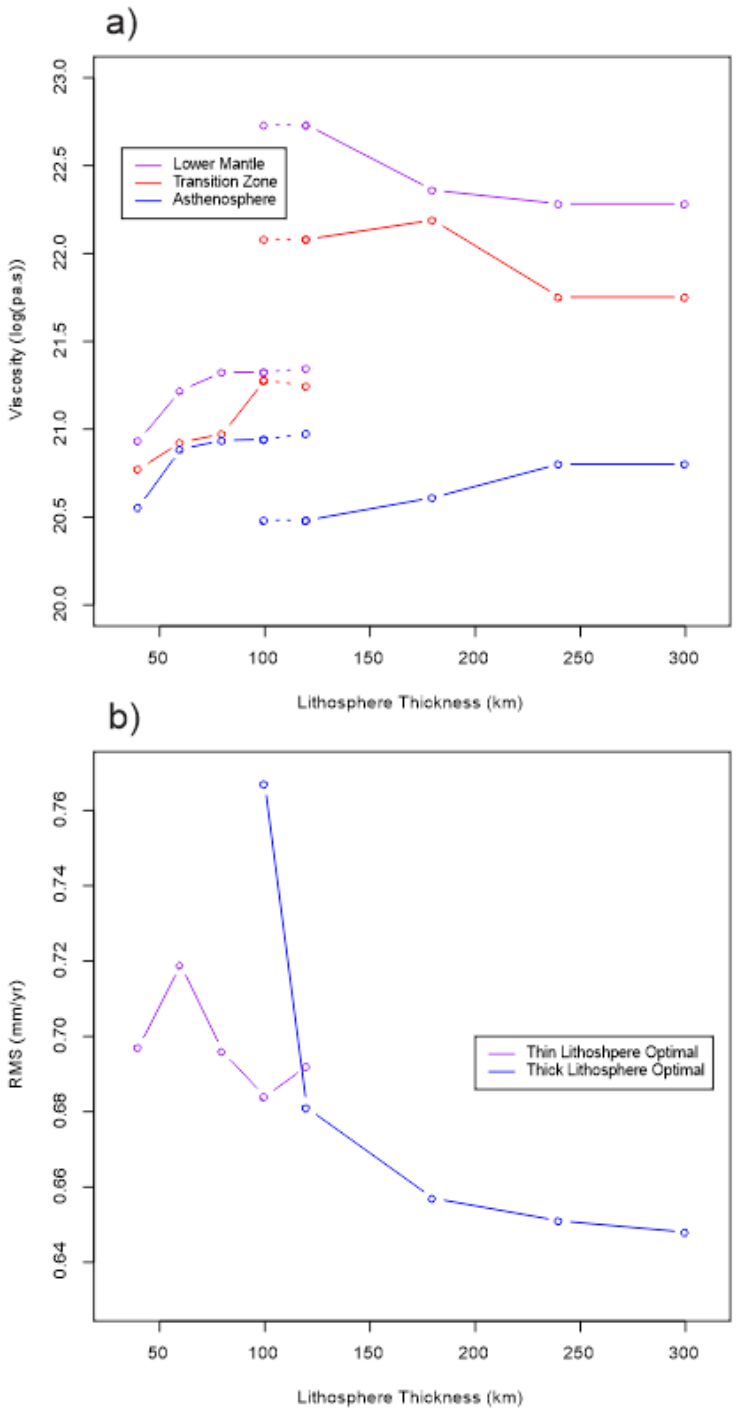

Figure 3.7: Horizontal minimization plots for a) viscosity profile and b) horizontal RMS, plotted against lithosphere thickness. The 100 and 120 km lithosphere local optimal RMS and viscosity profile are also shown for both plots. The thin lithosphere optimal refers to lithospheric thicknesses of 100 km and less and the thick lithosphere optimal refers to thicknesses of 120 km or greater.

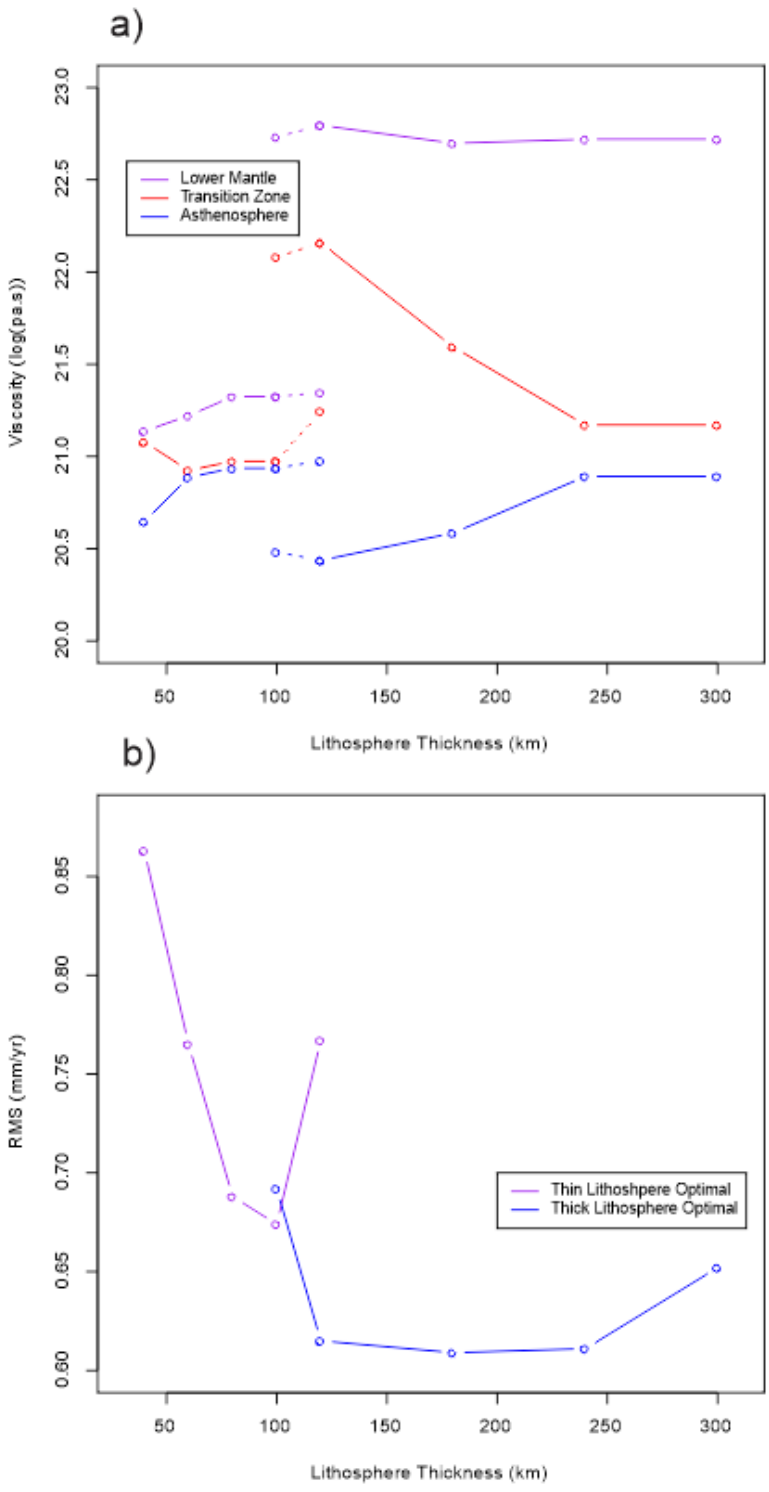

Figure 3.8: Combined minimization plots for a) viscosity profile and b) horizontal RMS, plotted against lithosphere thickness. The 100 and 120 km lithosphere local optimal RMS and viscosity profile are also shown for both plots. The thin lithosphere optima refers to lithospheric thicknesses of 100 km and less and the thick lithosphere optima refers to thicknesses of 120 km or greater.

The optimal viscosity profiles for the horizontal and combined minimizations at their respective local optima are very similar, with only minor changes to the transition zone viscosity in the thin lithosphere optima for the combined minimization. From the RMS plots, both the horizontal minimization and the combined minimization have a minimum RMS at 100 km, like the vertical, for the thin lithosphere branch, but the change in optimal profile obscured this. This thick lithosphere optimal profile does not appear to have a minimum for the horizontal and shares the same wide range of lithosphere thickness that produces the minimum RMS for the combined minimization.

With this exploration into the local optimal viscosity profiles, the thin lithosphere branch has a minimum RMS at 100 km thick lithosphere, as shown in the vertical (Figure 3.5b), horizontal (Figure 3.7b) and combined minimization (Figure 3.8b). In contrast, the thick lithosphere branch has a minimum RMS value across a broad range of lithospheric thicknesses (120 – 240 km) that is evident in the combined minimization (Figure 3.8b). The thick lithosphere minimization features viscosity profiles with much larger values for the lower mantle viscosity, around 5×10^{22} Pa·s, compared to 1-3 x 10^{21} Pa·s for the lower-mantle viscosity of the thin lithosphere branch.

The thin lithosphere profile and the relatively consistent vertical minimization viscosity profile are similar to well-documented viscosity profiles like VM1, VM5a, and VM7 (Peltier et al., 1976; Argus et al., 2014; Roy et al., 2017) which are used to accurately model relative sea-level data across North America. The thick lithosphere branch being only present in the horizontal and combined minimization might indicate that the horizontal crustal motions are more sensitive to lateral heterogeneity (Latychev et al., 2005a; Latychev et al., 2005b). Thus, for a laterally homogeneous study, the vertical crustal motions may be a better metric for determining the best-fitting model.

For comparison, crustal motion predictions are provided for the horizontal minimization (horizontal crustal motion, Figure 3.9), the vertical minimization (vertical crustal motion, Figure 3.10), and both horizontal and vertical crustal motion for the combined minimization (Figure 3.11).

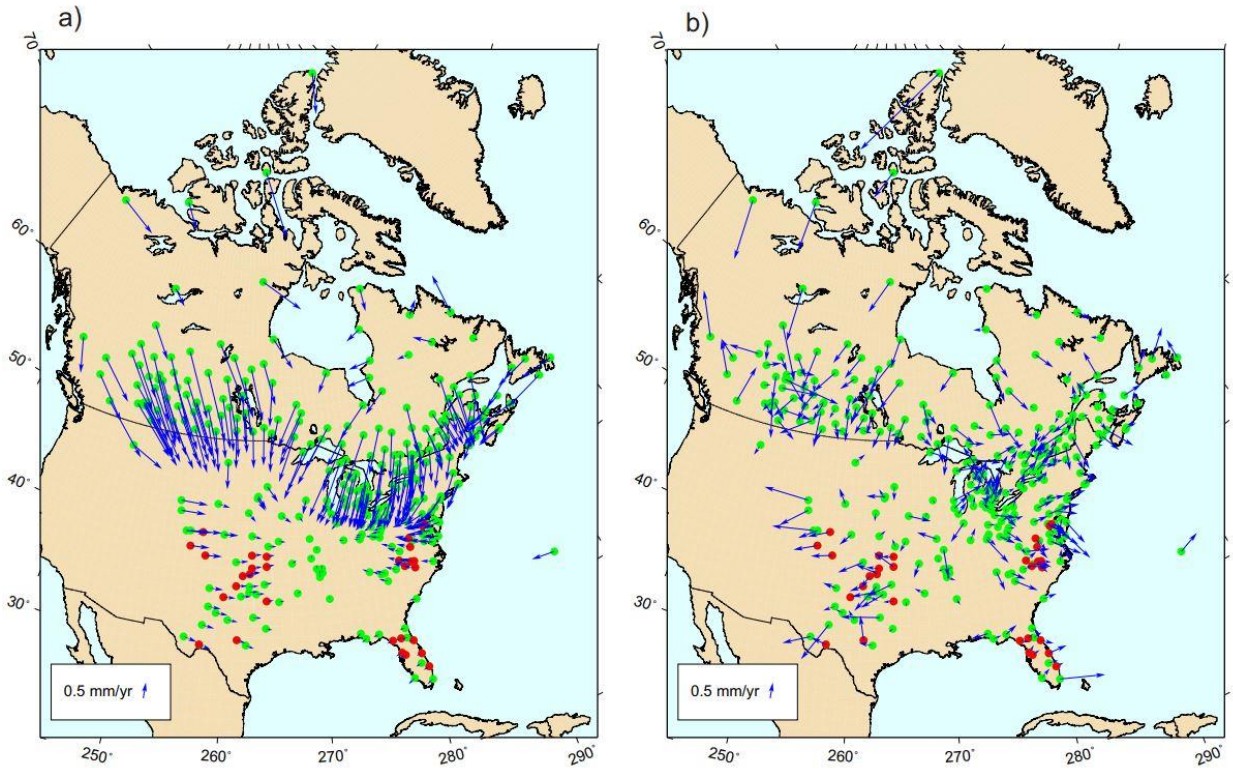

Figure 3.9: Horizontal motions for the smallest horizontal RMS for the 100 km lithosphere. a) predicted motions, b) residual velocities.

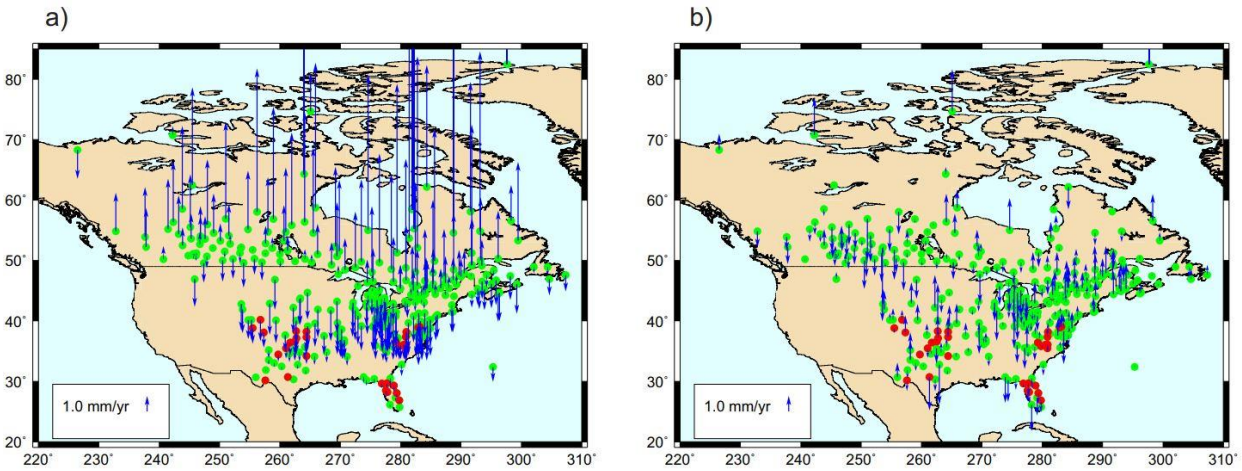

Figure 3.10: Vertical motions for the smallest vertical RMS for the 100 km lithosphere. a) predicted motions, b) residual velocities.

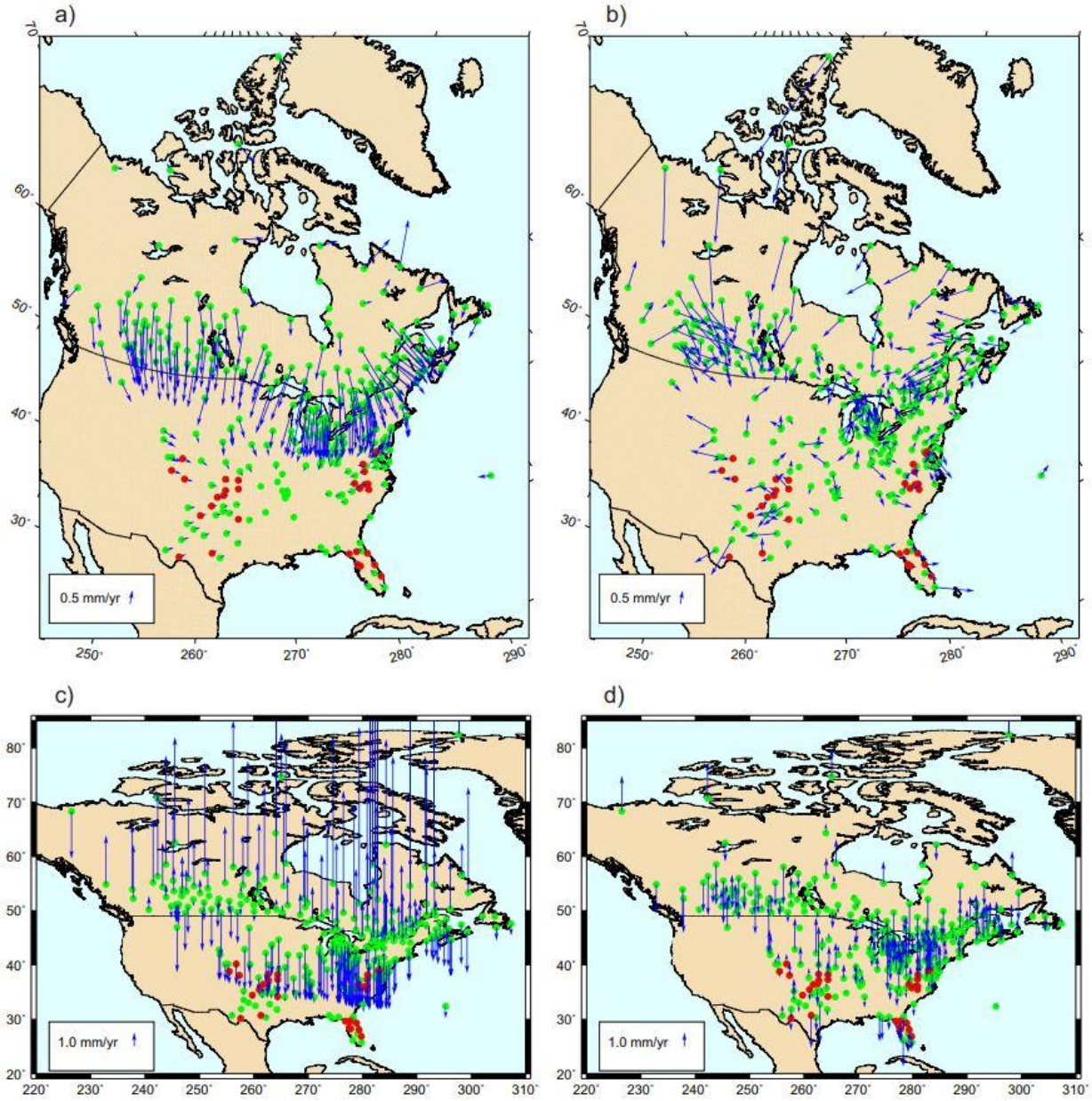

Figure 3.11: Vertical and horizontal motions for the smallest combined RMS for the 100 km lithosphere. a) and c) predicted horizontal and vertical motions. b) and d) are the corresponding residuals.

Table 3.4: RMS difference values for best models at 100 km.

	Horizontal RMS (mm/yr)	Vertical RMS (mm/yr)	Combined RMS (mm/yr)
Horizontal Minimization	0.684	N/A	N/A
Vertical Minimization	N/A	1.012	N/A
Combined Minimization	0.791	1.303	0.674

Figures 3.9 and 3.11 show that the horizontal crustal motion residuals share a very similar trend to what was shown in figure 3.2. The larger residuals are primarily in southern Canada and the residuals in the United States are oriented away from the central United States. The 100 km model shows a nearly 50% decrease in the RMS of the horizontal crustal motions (Table 3.4) when compared to the null model (Table 3.2), while VM1 has about a 30% decrease (Table 3.3).

Figures 3.10 and 3.11 show that the vertical crustal motion residuals between the vertical minimization and the combined minimization best models are visually quite different. The residuals around the Great Lakes for the vertical minimization are significantly improved while areas like Hudson Bay have very little change while the combined minimization has residuals that look very similar to the vertical residuals of VM1 (Figure 3.3b). For the vertical minimization model, there is around a 70% reduction in the RMS compared to the null model. This is an improvement to the 60% reduction from VM1, though not as much as the horizontal motions.

In contrast to the horizontal and vertical minimization, the combined minimization has very little visual difference to VM1 regarding the residual maps (comparing Figures 3.11b and d to Figure 3.2b and Figure 3.3b). Comparing the combined RMS values does not accurately quantify the difference as different weighting functions were used. For an accurate comparison, the horizontal and vertical RMS from the combined minimization should be compared to the horizontal and vertical RMS values of VM1 (Table 3.3).

Comparing the values from table 3.3 and table 3.4, the combined minimization model has a 10% improvement over VM1 for the horizontal motions, but the RMS for the vertical motions is very similar. The improvement in the vertical RMS is much less pronounced than the improvement in the horizontal RMS, but overall, the combined minimization model represents an improvement over VM1. This model

shows that, for the combined models, the best fitting model leaned towards improving the horizontal crustal motions at the potential expense of the vertical crustal motions.

Regardless of the minimization used, all models have substantial residuals. As a test, an additional GIA model set was created using a 4-layer model. A 4-layer model uses the same laterally homogeneous approximation as the 3-layer model but includes a high viscosity layer below the lithosphere, typically 30-40 km thick with a viscosity of 10^{22} Pa s (Argus et al., 2014; Argus et al., 2015; Peltier et al., 2015; Roy et al., 2015; Roy et al., 2017). This leads to a more complex Earth model. This added complexity has led to improved Earth models for North America, especially for the horizontal crustal motions (Argus et al., 2014). The generation of the 4-layer model follows the same parameter range and layer spacing described in table 3.1, but it uses the lithosphere thickness and high viscosity layer present in the VM7 profile (Roy et al., 2017). A comparison of the minimum RMS for both the vertical and horizontal is shown in figure 3.12.

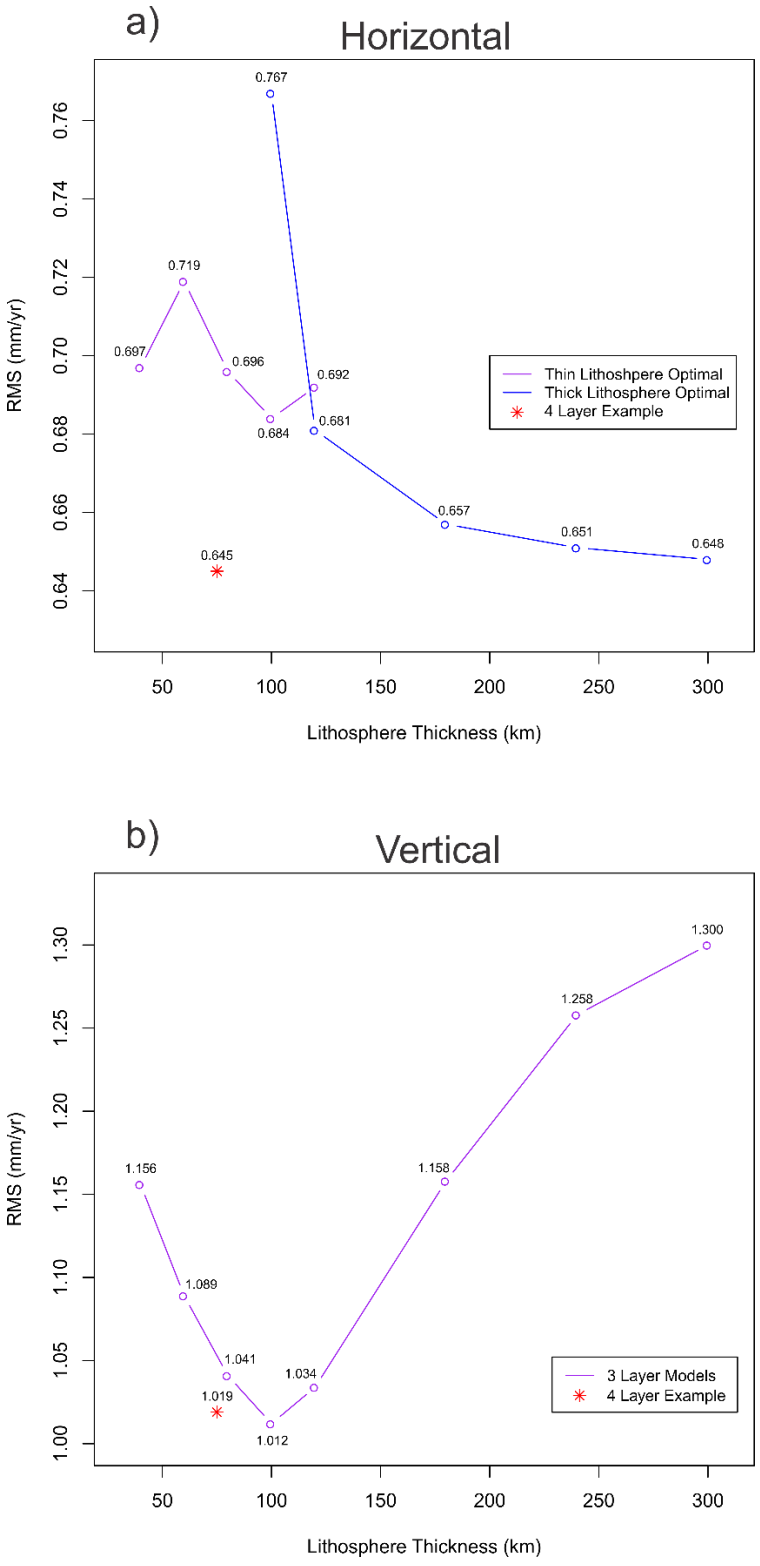

Figure 3.12: Minimum RMS vs lithosphere thickness for a) horizontal motions and b) vertical motions. The red star is the minimum RMS for the 4-layer model for the respective plot.

The 4-layer model produced a smaller RMS value relative to the 3-layer 80 km thick lithosphere models for both the vertical and horizontal crustal motions. The improvement for the horizontal motions is marked likely due to the horizontal motion's sensitivity to changes in shallow depth viscosities, while the improvement in the vertical motions is smaller. The 4-layer horizontal minimum is smaller than all 3-layer versions, while the vertical RMS is similar to the smallest 3-layer minimum. Even with the improvements that the 4-layer model brought, there is still a sizeable observed difference between the best models and the observed crustal motions. The RMS could likely be improved more by increasing the number of internal layers; however, these results suggest that laterally homogeneous Earth models will still lead to significant residual velocities. This points to the need for laterally heterogenous methods to capture more of the crustal motion response in North America (Zhong et al., 2003; Latychev et al., 2005a; Latychev et al., 2005b).

3.6 Conclusion

This chapter extensively explores the Earth model parameters (specifically, models of 3-layer mantle viscosity) to find the effects on predicted horizontal and vertical crustal motions for North America. Earth model parameters (3-layer mantle viscosity values and lithospheric thickness) were randomly generated for an extensive range of values, assuming a spherically symmetric Earth model. While the vertical crustal motions showed a very stable trend in optimal viscosity profile values across the tested lithosphere thicknesses, minimization of horizontal crustal motion residuals led to two different optimal viscosity profiles. The transition happens between 100 and 120 km, with the change in viscosities being close to an order of magnitude increase. The horizontal crustal motion residual showed no apparent minimum in RMS values, while the vertical crustal motions had a clear best model at 100 km thick lithosphere. Only when the local optimal viscosity profiles were determined and visualized did a best-fit model appear at the 100 km lithospheric thickness value, akin to the vertical.

The best-fitting model at 100 km thick lithosphere matches the observational data reasonably well, but there are still fairly large remaining residuals. A drawback of this analysis is that mantle viscosity profiles were limited to 3 layers. An examination of a 4-layer model (Argus et al., 2014; Roy et al., 2017) showed improvements to the vertical and especially the horizontal fit. Even with the improvement with the introduction of a 4-layer model, there was still a substantial horizontal motion residual. These residuals show the limitations associated with using the laterally homogeneous approximation.

The next step for improvement would be to use a laterally heterogenous finite element method of finding GIA models. This would allow lateral variations in Earth parameters such as lithosphere thickness. However, the approach to the study utilized in this chapter would have to be redesigned. Finite element models are computationally expensive and random generation of Earth models, and their responses, is not feasible. Instead, the results of this study could give a small selection of optimal viscosity profiles that can inform the selection of a limited number of 3-D earth models for comparison to the observations.

Chapter 4: Summary and Conclusion

4.1 Summary

This study explores the effects of Earth rheology on glacial isostatic adjustment (GIA) model predictions in North America. First, a new method (hybrid method), which addresses the issue of numerical singularities, is developed for finding the response of laterally homogeneous compressible Maxwell Earth models. With this method, the responses of thousands of Earth models were generated from randomly-generated viscosity profiles to explore the effects of Earth rheology on predicted vertical and horizontal motions. The study area includes most of North America east of the tectonically active western margin. In the study region, GIA model predictions are generally not in good agreement with observed horizontal crustal motions. The goal of this study was to examine the effects that the viscoelastic parameters (specifically, lithospheric thickness and 3-layer mantle viscosity profiles) have on crustal motion predictions and to explore the limitations of the laterally homogeneous Earth model assumption.

These best models were all found for a 100 km thick lithosphere. The vertical response specifically showed that the minimum root-mean-square (RMS) value was clearly at 100 km, but the horizontal and combined minima were not as clearly defined. As the lithosphere thickness increases from 100 to 120 km, the smallest residual models transitioned from one local optimal viscosity profile to another. Although the residuals continue to decrease for the horizontal and combined as the lithosphere thickness increases, the viscosity profiles of the best-fit models after the transition were significantly different compared to the profiles for the vertical response and the profiles before the transition. The horizontal and combined response have a defined minimum at 100 km akin to the vertical response on the thin-lithosphere branch. On the thick lithosphere branch, the RMS fits decrease with increasing lithospheric thickness.

Through the hybrid method, GIA models were found that could minimize the vertical and horizontal response residuals for a 100 km thick lithosphere to RMS values of 1.012 and 0.684 mm/yr, respectively, in comparison with the RMS values of observation residuals of 3.244 and 1.321 mm/yr for the same two components. The model that simultaneously minimized residuals for the vertical and horizontal responses, yields RMS 1.303 and 0.791 mm/yr, respectively, for these two components.

4.2 Comparison to Documented Profiles

The 100 km thick lithosphere of the best-fit models is intriguing as it lies in the middle of the optimal lithosphere thickness ranges from previous studies. Starting with VM1, introduced in 1976, the lithosphere thickness was set to 120 km (Peltier et al., 1976). VM1 was used for a number of years until the introduction of VM2 and VM3, which both had a lithosphere thickness of 90 km (Peltier, 1996; Peltier, 2002). In this transition from VM1 to VM2/VM3, several studies experimented with lithosphere thicknesses beyond 200 km (Peltier, 1984; Peltier, 1986; James et al., 1990). With the introduction of space geodesy data, the first viscosity profile that included a high viscosity layer was introduced, denoted as VM5a (Argus et al., 2015; Peltier et al., 2015). VM5a was unique as it used a 60 km thick lithosphere, which was far thinner than the previous studies, but also included a high viscosity sub-lithospheric layer. This sub-lithospheric layer's viscosity is 40 km thick and was set at 10^{22} Pa·s, 1 order of magnitude greater than the subjacent layer's viscosity. Shortly after VM5a was introduced, an updated viscosity profile VM6 was presented, with a lithosphere thickness at 90 km akin to VM2 and VM3 while including the sub-lithospheric layer, this time only 30 km thick (Roy et al., 2015). Finally, the most recent version of the VMx profiles is VM7 which has a lithosphere thickness of 75 km and has the same sub-lithospheric layer as VM5a of 40 km thickness and viscosity 10^{22} Pa s (Roy et al., 2017).

The lithosphere thickness (100 km) of our best-fitting model falls within the range of lithospheric thicknesses of numerous published papers (Peltier et al., 1976; Peltier, 1996; Peltier, 2002; Roy et al.,

2015) and indicates general consistency with previous studies. A 100 km thick lithosphere is between VM1 (120 km) and VM7 (95 km) and is almost the same as VM2, VM3, and VM6. Smaller and larger lithospheric thicknesses were explored, and it was found that our results worsened overall if the thickness went below 80 km thickness. Above 120 km thickness the vertical response degrades, but the horizontal response improves. As explored in the discussion section of Chapter 3, this improvement to the horizontal motions at 120+ km lithosphere thickness comes with an extreme shift away from the viscosity profile present in the 100 km model. This shifted viscosity profile significantly differs from previously published inferences into mantle viscosity; coupled with a visible minimum in the horizontal response when only considering the 100 km optimal viscosity range, this leads to the argument that the best models for the horizontal motions are also at 100 km.

The best models were relatively consistent in their viscosity profiles when the lithosphere thickness was between 60 km and 100 km, so VM5a's thinner lithosphere did not produce significantly different viscosity profiles. Both this study and Peltier's 2015 paper used GNSS data to refine the optimal models, probably contributing to the consistency between our results. Models with lithosphere thicknesses larger than 120 km produce viscosity profiles that were quite different when considering the horizontal motions. This change in the optimal viscosity profile points towards how sensitive the horizontal displacements are to the lithosphere thickness and viscosity profile, more so than the vertical (James et al., 1990; Latychev et al., 2005a; Latychev et al., 2005b).

This study's best models all have a 100 km thick lithosphere, which is relatively close to most of the documented VMx profiles, but the viscosity profiles corresponding to our best models differ from the VMx profiles. To illustrate this difference, figure 4.1 shows the viscosity profiles of the best model for 100 km plotted with the VMx viscosity profiles.

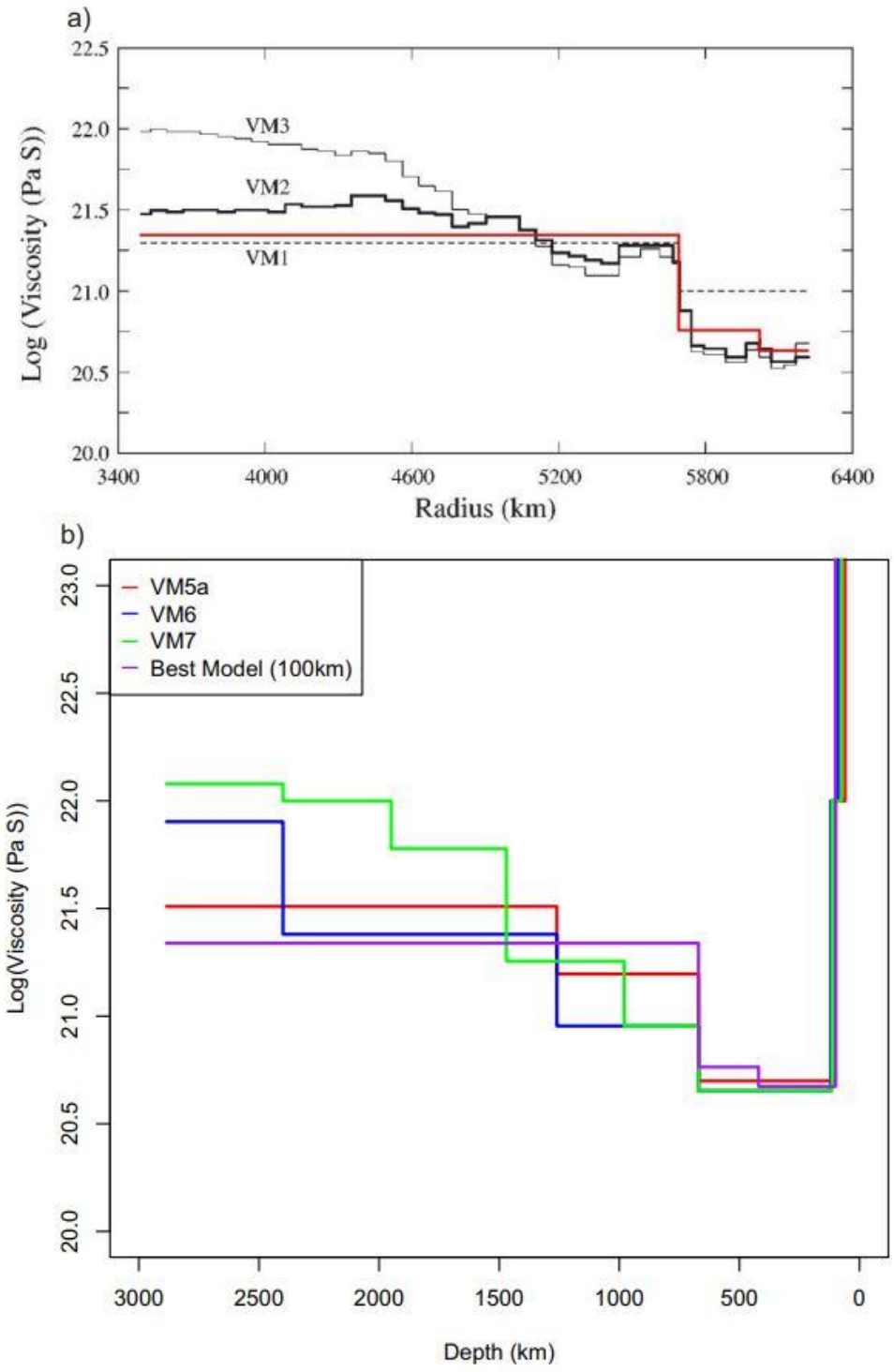

Figure 4.1: Viscosity profiles for a) best fitting model for vertical crustal motions at 100 km (red line) compared to VM1, VM2, and VM3 (Adapted from figure 1 of Peltier, 2002), and b) best fitting model for vertical crustal motions at 100 km (purple line) compared to VM5a, VM6, and VM7. (Peltier et al., 1976; Peltier, 1996; Peltier, 2002; Argus et al., 2015; Roy et al., 2015; Roy et al., 2017)

The best fitting viscosity profile is similar to all VMx viscosity profiles except VM1 at shallow depths (420 km depth and shallower), but at greater depths our best fitting viscosity is more similar to VM1 than other VMx profiles. This difference likely arises from how this study stratified the lower mantle, as there was only one mantle viscosity layer for the lower mantle, similar to VM1. All other viscosity profiles in figure 4.1 have additional layers between 670 km depth and the outer core-mantle boundary. VM5a, VM6, and VM7 also have a 40 km thick high viscosity layer below the lithosphere which, for VM5a, improved residuals of both the vertical and horizontal crustal motions, as discussed in Chapter 3.

As discussed in Chapter 3, there is a sharp transition between viscosity profiles that produced the smallest horizontal RMS between 100 km and 120 km. Figure 4.2 highlights the magnitude of the difference between the thick lithosphere viscosity profiles, the 100 km thick best-fitting model, and the more recent VMx viscosity profiles.

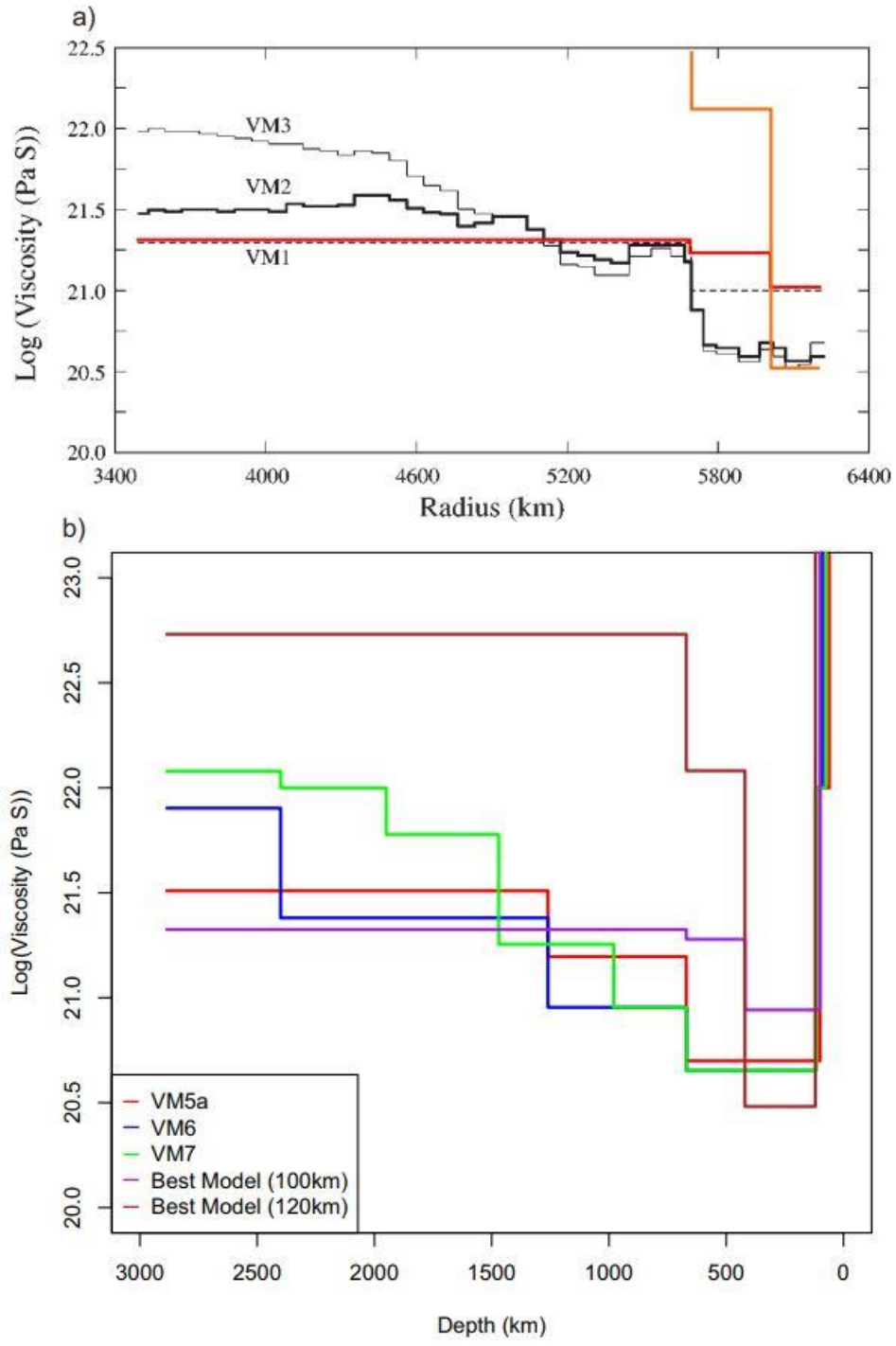

Figure 4.2*:* Viscosity profiles for a) best fitting model for horizontal crustal motions at 100 km (red line) and 120 km (orange line) compared to VM1, VM2, and VM3 (Adapted from figure 1 of Peltier, 2002), and b) best fitting model for vertical crustal motions at 100 km (purple line) and 120 km (brown line) compared to VM5a, VM6, and VM7. (Peltier et al., 1976; Peltier, 1996; Peltier, 2002; Argus et al., 2015; Roy et al., 2015; Roy et al., 2017)

Unlike in figure 4.1a, the best 100 km thick viscosity profile for minimizing the horizontal crustal motions does not agree with most of the VMx profiles. Only VM1 is similar to this profile for depths above 420 km and below 670 km. The best 120 km thick viscosity profile however is very different to all versions of the VMx profiles regardless of the depth. The viscosity above 420 km is similar to VM2 and VM3, but at depths greater than 420 km the viscosity increases far beyond the range of all the VMx profiles.

4.3 Potential Sources of Uncertainty and Next Steps

Despite the extensive search through Earth parameter space, our best models still have significant residuals. A number of factors could contribute to the residuals. The first potential source is the generation of the Earth model responses. The hybrid method, shown to be the superior method in Chapter 2, may still have remaining errors arising from the application of the collocation method to the residuals produced from the normal mode method. However, the hybrid method does retain as much modal structure as possible and fits the computed s-dependent Love numbers well, so the remaining error of the predicted motions is minimized and this is not thought to be a significant contributor to the residuals.

Another potentially important contributor to the large residuals is that some processes that may contribute significantly to crustal motion have not been considered. Ongoing ice mass loss, hydrological effects, and plate tectonics may contribute to crustal motion. Culling more sights in the north and the west would reduce the influence of these phenomena and potentially reduce the overall residuals. Hydrological effects from the Great Lakes and elsewhere would likely need to be removed from the observational dataset as it would be unrealistic to cull that many sites for GIA modeling. Alternatively, a joint analysis of hydrological effects and GIA would reveal the dependencies and sensitivities of the two processes.

Another reason that observed velocities are not fully fit may stem from the number of viscosity layers used. This study focused on an extensive exploration of a 3-layer viscosity profile. The number of layers chosen for this study was deliberate, as it was enough to stratify the Earth's rheology while not requiring an excessive number of models to properly explore the viscosity space. This approach contrasts with other studies of North American crustal motion models that present viscosity profiles with more than 3 layers. For the purposes of finding the smallest possible residuals, a 3-layer exploration with a 40 km thick sub-lithospheric high viscosity layer would produce smaller residuals, as shown in Chapter 3. A larger number of layers might reduce the residuals further.

As discussed in chapter 3, the likely reason for the large residuals is due to the laterally homogeneous assumption inherent in the numerical method. The numerical methods used in this report require that the viscosity profile only varies with depth. Seismic velocity profiles generated using seismic tomographic techniques reveal lateral variations in seismic velocity (Ritsema et al., 2011; Audet and Burgmann, 2011; Schaeffer et al., 2013; Auer et al., 2014; French et al., 2014; Clouzet et al., 2018). An example of these lateral variations in the mantle velocity is shown in figure 4.3.

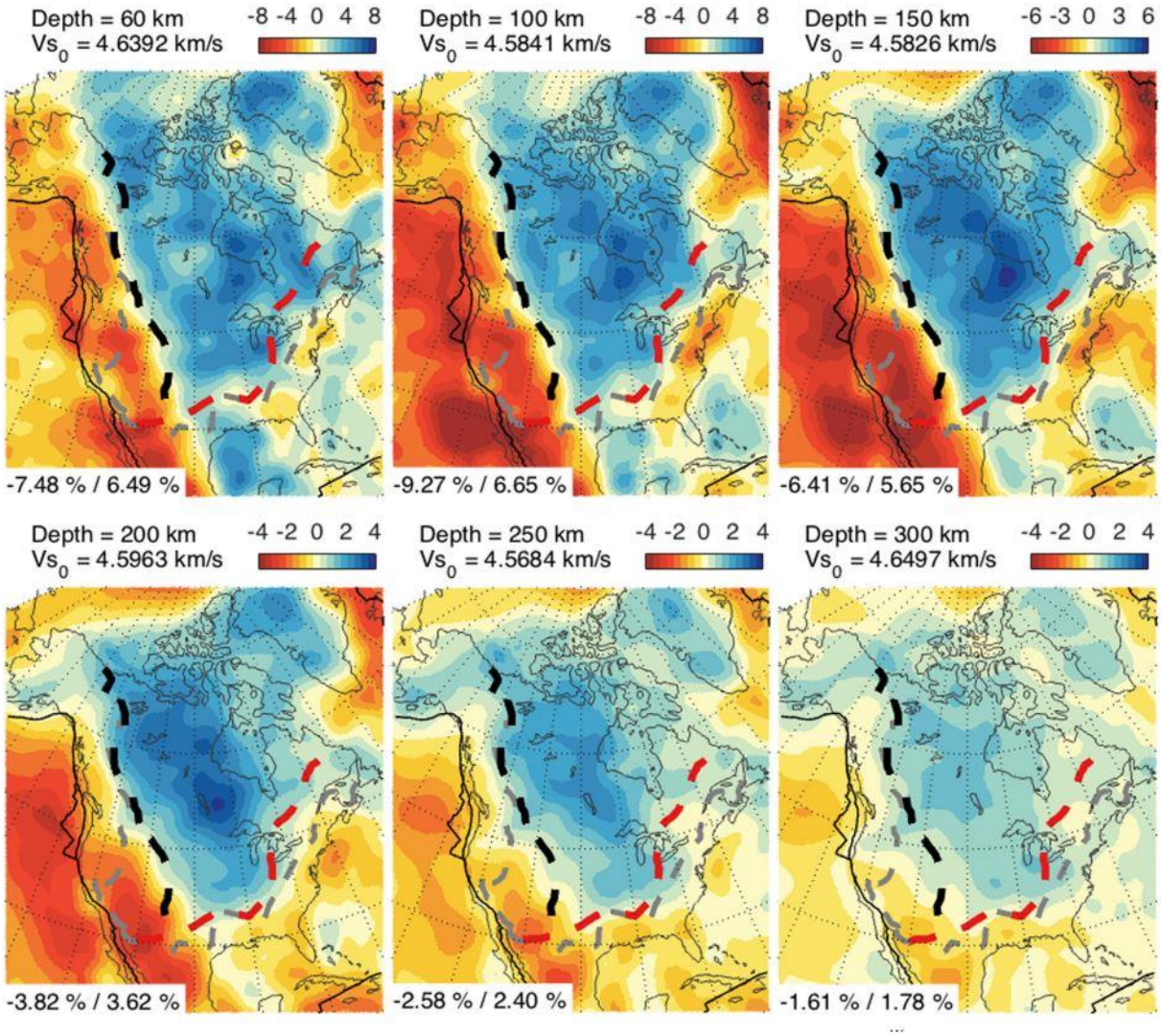

Figure 4.3: 3D isotropic shear wave velocity structure as relative perturbations from a regional mean at different depths across North America. The black dashed line refers to the Rocky Mountain front, the grey line refers to the western and eastern breakup lines, and the red dashed line refers to the Grenville front. Adapted from figure 8 of Clouzet et al., 2018.

At all depths shown, there is some lateral variation in the velocity structure, indicating lateral variation in the mantle viscosity profile. The laterally homogeneous models used in this study are unable to capture this lateral variation.

Though this study describes an extensive exploration of mantle viscosity and lithosphere thickness for North American GIA model predictions, the lack of a consistent minimum for the horizontal and combined residuals, as well as the relatively large residuals for best-fitting models, suggests the

need for further analysis. Two approaches could be taken to expand on this study. The first is to repeat this experiment with a greater number of mantle viscosity layers. Though this study argues that there would only be a minor improvement to the residuals, there is still value in exploring the degree to which a more stratified viscosity profile would improve the fit to the observed velocities.

Most recently published viscosity profiles have more than 3 layers, including the most recent VM7, which has 7 layers. It is possible that an improved model with smaller residuals could be found doing this similar search through viscosity space with additional layers, but the layering would need to carefully considered due to the depth sensitivity of GIA model predictions (Mitrovica and Peltier, 1991b; Lau et al., 2016) while also being prohibitively expensive, as the number of models required to search through a 7 layered viscosity space would be orders of magnitude greater than what was used in this study. The approach taken in this report would need to be reworked into an inverse procedure in order to extend this exploration to 7 or more viscosity layers.

The other step that could be taken would be to explicitly incorporate lateral heterogeneity into the Earth models. A laterally heterogenous model would result in a more accurate representation of lithospheric and upper mantle structure in North America and might lead to more robust inferences of Earth rheology. However, the methodology used in this study would have to be radically changed. A random search through viscosity space akin to what was done in this study would not be feasible for laterally heterogenous models. There are several reasons for this, but the biggest one would be the computational requirements. Finite element modeling is far more computationally expensive than the laterally homogeneous methods used in this study. Couple that with an increased amount of required models to effectively explore laterally heterogenous viscosity space through random search, and the amount of time to recreate this experiment with finite element modeling would be prohibitive. A study like this would not be able to do an extensive search through viscosity space by randomly choosing values; instead, earth models would need to be developed by synthesizing data from many geophysical

sources and experimenting with the parameters within those constraints. The laterally homogeneous results presented here would provide important input for assigning background mantle viscosity and lithospheric thickness values.

References

Argus F.D., Peltier W.R., Drummond R., Moore A.W., 2014, *The Antarctica component of Postglacial Rebound Model ICE-6G_C (VM5a) Based on GPS Positioning, Exposure Age Dating of Ice Thickness, and Relative Sea Level Histories*, Geophysical Journal International, Vol 198, doi:10.1093/gji/ggu140

Argus F.D., Ratliff B., DeMets C., Borsa A.A., Wiese D.N., Blewitt G., Crowley J.W., Martens H.R., Kreemer C., Landerer F.W., 2020, *Rise of Great Lakes Surface Water, Sinking of the Upper Midwest of the United States, and Viscous Collapse of the Forebulge of the Former Laurentide Ice Sheet,* Journal of Geophysical Research: Solid Earth, Vol 125, doi: 10.1029/2020JB019739

Audet P., Burgmann R., 2011, *Dominate Role of Tectonic Inheritance in Super Continent Cycles,* Nature Geoscience Letters, Vol 4, doi: 110.1038/NGEO1080

Auer L., Boschi L., Becker T.W., Nissen-Meyer T., Giardini D., 2014, *Savani: A Variable Resolution Whole-Mantle Model of Anisotropic Shear Velocity Variations Based on Multiple Data Sets,* Journal of Geophysical Research: Solid Earth, Vol 119, doi: 10.1002/2013JB010773

Backus G.E., 1967, *Converting Vector and Tensor Equations to Scalar Equations in Spherical Coordinates*, Geophysical Journal International, Vol 13, https://doi-org/10.1111/j.1365-246X.1967.tb02147.x

Bland D.R., 1960, *The Theory of Linear Viscoelasticity*, Pergamon Press, Oxford

Blewitt G., Hammond W.C., Kreemer C., 2018, *Harnessing the GPS Data Explosion for Interdisciplinary Science*, EOS, Vol 99, https://doi.org/10.1029/2018EO104623.

Carrera G., Vanicek P., Craymer M.R., 1991, *The Compilation of a Map of Recent Vertical Crustal Movements in Canada, Department of Surveying Engineering Technical Report No. 153*, University of New Brunswick, Fredericton, N.B., Canada

Cazenave A., Dominh K., Guinehut S., Berthier E., Llovel W., Ramillien G., Ablain M., Larnicol G., 2009, *Sea Level Budget Over 2003-2008: A Reevaluation from GRACE Space Gravimetery, Satellite Altimetry and Argo*, Global and Planetary Change, Vol 65, doi:10.1016/j.gloplacha.2008.10.004

Coulson S., Lubeck M., Mitrovica J.X., Powell E., Davis J.L, Hoggard M.J., 2021, *The Global Fingerprint of Modern Ice-Mass Loss on 3-D Crustal Motion*, Geophysical Research Letters, Vol 48, doi:10.1029/2021GL095477

Dahlen F.A., 1976, *The Passive Influence of the Oceans Upon the Rotation of the Earth,* Geophysical Journal International: Royal Astronomical Society, Vol 46, doi:10.1111/j.1365-246X.1976.tb04163.x

DeGrandpre G., and Freymueller J.T., 2019, *Vertical Velocities, Glacial Isostatic Adjustment, and Earth Structure of Northern and Western Alaska Based on Repeat GPS Measurements*, Journal of Geophysical Research: Solid Earth, Vol 124, doi:10.1029/2018JB017163

Dietrich R., Ivins E.R., Casassa G., Lange H., Wendt J., Fritsche M., *Rapid Crustal Uplift in Patagonia Due to Enhanced Ice Loss*, Earth and Planetary Science Letters, Vol 289, doi:10.1016/j.epsl.2009.10.021

Dziewonski A.M., and Anderson D.L., 1981, *Preliminary Reference Earth Model,* Physics of the Earth and Planetary Interiors, Vol 25, doi:10.1016/0031-9201(81)90046-7

Elliott J.L., Larsen C.F., Freymueller J.T., Motyke R.J., 2010, *Tectonic Block Motion and Glacial Isostatic Adjustment in Southeast Alaska and Adjacent Canada Constrained by GPS Measurements*, Journal of Geophysical Research, Vol 115, doi:1029/2009JB007139

Farrell W.R., Clark J.A., 1976, *On Postglacial Sea Level*, Geophysical Journal of the Royal Astronomical Society, Vol 46, https://doi-org/10.1111/j.1365-246X.1976.tb01252.x

French S.W., Romanowicz B.A., 2014, *Whole-Mantle Radially Anisotropic Shear Velocity Structure from Spectral-Element Waveform Tomography,* Geophysical Journal International, Vol 199, doi: 10.1093/gji/ggu334

Hampel A., Luke J., Krause T., Hetzel R., 2019, *Finite-Element Modeling of Glacial Isostatic Adjustment (GIA): Use of Elastic Foundations at Material Boundaries Versus the Geometrically Non-Linear Formulation,* Computers and Geosciences, Vol 122, doi:10.1016/j.cageo.2018.08.002

James T.S., 1991, *Post-Glacial Deformation*, PhD Dissertation, Princeton University, Princeton, New Jersey

James T.S., Clague J.J., Wang K. and Hutchinson I., 2000, *Postglacial rebound at the northern Cascadia subduction zone*, Quaternary Science Reviews, Vol 19, https://doi.org/10.1016/S0277-37910000076-7

James T.S., Gowan E.J., Hutchinson I., Clague J.J., Barries V.J., Conway K.M., 2009*, Sea-level Change and Paleogeographic Reconstructions*, *Southern Vancouver Island, British Columbia, Canada,* Quaternary Science Reviews, Vol 28, https://doi.org/10.1016/j.quascirev.2008.12.022

James T.S., Henton J.A., Leonard L.J., Darlington A., Forbes D.L., Craymer M., 2014, *Realtive Sea-Level Projections in Canada and the Adjacent Mainland United States,* Geological Survey of Canada, Open File 7737, doi:10.4095/295574

James T.S. and Ivins E.R., 1998, *Predictions of Antarctic Crustal Motions Driven by Present-Day Ice Sheet Evolution and by Isostatic Memory of the Last Glacial Maximum*, Journal of Geophysical Research, Vol 103, doi:10.1029/97JB03539

James T.S. and Lambert A., 1993, *A Comparison of VLBI Data with the ICE-3G Glacial Rebound Model*, Geophysical Research Letters, Vol 20, https:/doi-org/10.1029/93GL00865

James T.S. and Morgan W.J., 1990, *Horizontal Motions Due to Post-Glacial Rebound*, Geophysical Research Letters, Vol 17, https://doi-org/10.1029/GL017i007p00957

Kendall R.A., Mitrovica J.X., Milne G.A., 2005, *On Post-Glacial Sea Level – II. Numerical Formulation and Comparative Results on Spherically Symmetric Models,* Geophysical Journal International, Vol 161, https://doi.org/10.1111/j.1365-246X.2005.02553.x

Klemann V., Wu P., Wolf D., 2003, *Compressible Viscoelasticity: Stability of Solution for Homogeneous Plane-Earth Models,* Geophysical Journal International, Vol 153, doi:10.1049/j.1365-246X.2003.01920.x

Koohzare A., Vanicek P., Santos M., 2008, *Pattern of Recent Vertical Crustal Movements in Canada*, Journal of Geodynamics, Vol 45, doi:10.106/j.jog.2007.08.001

Kreemer C., Blewitt G., Klein E.C., 2014, *A Geodetic Plate Motion and Global Strain Rate Model*, Geochemistry, Geophysics, Geosystems, Vol 15, https://doi.org/10.1002/2014GC005407

Kreemer C., Hammond W.C., Glewitt G., 2018, *A Robust Estimation of the 3-D Intraplate Deformation of North American Plate from GPS,* Journal of Geophysical Research: Solid Earth, Vol 123, https://doi.org/10.1029/2017JB015257

Latychev K., Mitrovica J.X., Tamisiea M.E., Tromp J., Moucha R., 2005a, *Influence of Lithospheric Thickness Variations on 3-D Crustal Velocities Due to Glacial Isostatic Adjustment,* Geophysical Research Letters, Vol 32, doi:10.1029/2004GL021454

Latychev K., Mitrovica J.X., Tromp J., Tamisiea M.E., Komatitsch D., Christara C.C., 2005b, *Glacial Isostatic Adjustmetn on 3-D Earth Models: a Finite-Volume Formulation,* Geophysical Journal International, Vol 161, doi:10.1111/j1365-246X.2005.02536.x

Lau H.C.P., Mitrovica J.X., Austermann J., Crawford O., Al-Attar D., Latychev K., 2016, *Inferences of Mantle Viscosity Based on Ice Age Data Sets: Radial Structure,* Journal of Geophysical Research: Solid Earth, Vol 121, doi: 10.1002/2016JB013043

Lewis M.C.F., Breckenridge A.J., Teller J.T., 2021, *Reconstruction of Isostatically Adjusted Paleo-strandlines Along the Southern Margin of the Laurentide Ice Sheet in the Great Lakes, Lake Agassiz, and Champlain Sea Basin*, Canadian Journal of Earth Science, Vol 59, dx.doi.org/10.1139/cjes-2021-0005

Li T., Wu P., Steffen H., Wang H., 2018, *In Search of Laterally Heterogenous Viscosity Models of Glacial Isostatic Adjustment with the ICE-6G_C Global Ice History Model,* Geophysical Journal International, Vol 214, doi:10.1093/gjo/ggy181

Lombard A., Garcia D., Ramillien G., Cazenave A., Biancale R., Lemoine J.M., Flechtner, F., Schmidt R., Ishii M., 2007, *Estimation of Steric Sea Level Variations from Combined GRACE and Jason-1 Data*, Earth and Planetary Science Letters, Vol 254, doi:10.1016/j.epsl.2006.11.035

Martinec Z., 2000, *Spectral-Finite Element Approach to Three-Dimensional Viscoelastic Relaxation in a Spherical Earth,* Geophysics Journal International, Vol 142, doi:10.1046/j.1365-246x.2000.00138.x

Martinec Z., Klemann V., van der Wal W., Riva R.E.M., Spada G., Sun Y., Melini D., Kachuck S.B., Barletta V., Simon K., A G., James T.S., 2018, *A Benchmark Study of Numerical Implementations of the Sea Level Equation in GIA Modeling,* Geophysical Journal International, Vol 215, doi: 10.1093/gji/ggy280

Milne G.A., Davis J.L., Mitrovica J.X., Scherneck H.G., Johansson J.M., Vermeer M., Koivula H., 2001, *Space-Geodetic Constraints on Glacial Isostatic Adjustment in Fennoscandia*, Vol 291, Geophysical Journal International, doi:10.1126/science.1057022

Mitrovica J.X., Davis J.L., Shapiro I.I., 1993, *Constraining Proposed Combinations of Ice History and Earth Rheology Using VLBI Determined Baseline Length Rates in North America*, Geophysical Research Letters, Vol 20, https://doi-org/10.1029/93GL02043

Mitrovica J.X., Milne G.A., 2003, *On Post-Glacial Sea Level: I. General Theory*, Geophysical Journal International, Vol 154, https://doi-org/10.1046/j.1365-246X.2003.01942.x

Mitrovica J.X. and Peltier W.R., 1991a, *On Postglacial Geoid and Subsidence Over the Equation Oceans*, Journal of Geophysical Research, Vol 96, https://doi-org/10.1029/91JB01284

Mitrovica J.X. and Peltier W.R., 1991b, *A Complete Formalism for the Inversion Post-Glacial Rebound Data: Resolving Power Analysis,* Geophysical Journal International, Vol 104, doi: 10.1111/j.1365-246X.1991.tb02511.x

Mitrovica J.X. and Peltier W.R., 1992, *A Comparison of Methods for the Inversion of Viscoelastic Relaxation Spectra*, Geophysical Journal International, Vol 108, 410-414, doi:10.1111/j.1365-246X.1992.tb04623.x

Ojo A.O., Kao H., Jiang Y., Craymer M., Henton J., 2021, *Strain Accumulation on Release Rate in Canada: Implications for Long-Term Crustal Deformation and Earthquake Hazards*, Journal of Geophysical Research: Solid Earth, Vol 126 , https://doi.org/10.1029/2020JB020529

Peltier W.R., 1974, *The Impulse Response of a Maxwell Earth*, Reviews of Geophysics, Vol 12, https://doi-org/10.1029/RG012i004p00649

Peltier W.R., 1976, *Glacial-Isostatic Adjustment-II. The Inverse Problem,* Journal of Geophysical Journal of the Royal Astronomical Society, 10.1111/j.1365-246X.1976.tb01253.x

Peltier W.R., 1984, *The Thickness of the Continental Lithosphere,* Journal of Geophysical Research, Vol 89, https://doi.org/101029/JB089iB13p11303

Peltier W.R., 1986, *Deglaciation-induced Vertical Motion of the North-American Continent and Transient Lower Mantle Rheology*, Journal of Geophysical Research: Solid Earth, Vol 91, https://doi.org/10.1029/JB091iB09p09099

Peltier W.R., 1996, *Mantle Viscosity and Ice-Age Sheet Topography*, Science, Vol 273, doi: 10.1126/science.273.5280.1359

Peltier W.R., 2002, *Global Glacial Isostatic Adjustment: Palaeogeodetic and Space-Geodetic Tests of the ICE-4G (VM2) Model,* Journal of Quaternary Science, Vol 17, https://doi.org./10.1002/jqs.713

Peltier W.R., Argus D.F., Drummond R., 2015*, Space Geodesy Constrains Ice-Age Terminal Deglaciation: The Global ICE6G_C (VM5a) model*, Journal of Geophysical Research: Solid Earth, Vol 120, https://doi.org/10.1002/2014JB011176

Richter A., Ivins E., Lange H., Mendoza L., Schroder L., Hormaechea J.L., Casassa G., Marderwald E., Fritsche M., Perdomo R., Horwath M., Dietrich R., 2016, *Crustal Deformation Across the Southern Patagonian Icefield Observed by GNSS*, Earth and Planetary Science Letters, Vol 452, doi:10.106/j.epsl.2016.07.042

Ritsema J., Deuss A., Heijst H.J., Woodhouse J.H., 2011, *S40RTS: A Degree-40 Shear-Velocity Model for the Mantle from New Rayleigh Wave Dispersion, Teleseismic Traveltime and Normal-Mode Splitting Function Measurements,* Geophysical Journal International, Vol 184, doi: 10.1111/j.1365-246X.2010.04884.x

Riva R.E.M., Frederikse T., King M.A., Marzeion B., van den Broeke M.R., 2017, *Brief Communication: The Global Signature of Post-1900 Land Ice Wastage on Vertical Land Motion,* The Cryosphere, Vol 11, doi:10.5194/tc-11-1327-2017

Robin C.M.I., Craymer M., Ferland R., James T.S., Lapelle E., Piraszewski M., Zhoa Y., 2020, *NAD83v70VG: A New National Crustal Velocity Model for Canada,* Geomatics Canada, Open File 0062, https://doi.org/10.4095/327592

Roy K., Peltier W.R., 2015, *Glacial Isostatic Adjustment, Relative Sea Level History and Mantle Viscosity: Reconciling Relative Sea Level Model Predictions for the U.S. East Coast with Geological Constraints,* Geophysical Journal International, Vol 201, doi:10.1093/gji/ggv066

Roy K., Peltier W.R., 2017, *Space-Geodetic and Water Level Gauge Constraints on Continental Uplift and Tilting Over North America: Regional Convergence of the ICE-6G_C (VM5a/VM6) Models*, Geophysical Journal International, Vol 210, doi:10.1093/gji/ggx156

Roy K., Peltier W.R., 2018, *Relative Sea Level om the Western Mediterranean Basin: A Regional Test of the ICE-7C_NA (VM7) Model and a Constraint on Late Holocene Antarctic Deglaciation,* Quaternary Science Reviews, Vol 183, doi:10.1016/j.quascirev.2017.12.021

Schaeffer A.J., Lebedev S., 2013, *Global Shear Speed Structure of the Upper Mantle and Transition Zone,* Geophysical Journal International, Vol 194, doi: 10.1093/gji/ggt095

Sella G.F., Stein S., Dixon T.H., Craymer M., James T.S., Stephane M., Dokka R.K., 2007, *Observation of Glacial Isostatic Adjustment in "Stable" North America with GPS*, Geophysical Research Letters, Vol 34, doi:10.1029/2006GL027081

Simon K.M., 2014, *Improved Glacial Isostatic Adjustment for Northern Canada*, PhD thesis, University of Victoria, Victoria, Canada

Simon K.M., James T.S., Dyke A.S., 2015, *A New Glacial Isostatic Adjustment Model for the Innuitian Ice Sheet,* Quaternary Science Reviews, Vol 119, httos://doi.org/10.1016/j.quascirev.2015.04.007

Simon K.M., James T.S., Henton J.A., Dyke A.S., 2016, *A Glacial Isostatic Adjustment Model for the Central and Northern Laurentide Ice Sheet Based on Relative Sea Level and GPS Measurements*, Geophysical Journal International, Vol 205, doi:10.1093/gji/ggw103

Spada G., Barletta V.R., Klemann V., Riva R.E.M., Martinec Z., Gasperini P., Lund B., Wolf D., Vermeersen L.L.A., King M.A., 2011, *A Benchmark Study for Glacial Isostatic Adjustment Codes,* Geophysical Journal International, Vol 185, doi: 10.111/j.1365-246X.2001.04952.x

Steffen H., Kaufmann G., Wu P., 2006, *Three-Dimensional Finite-Element Modeling of the Glacial Isostatic Adjustment in Fennoscandia,* Earth and Planetary Science Letters, Vol 250, doi: 10.1016/j.epsl.2006.08.003

Steffen R., Wu P., Steffen H., Eaton D.W., 2014, *On the Implementation of Faults in Finite-Element Glacial Isostatic Adjustment Models*, Computers and Geoscience, Vol 62, httpd://doi.org/10.10116/j.cageo.2013.06.012

Tamisiea M.E., Mitrovica J.X., Tromp J., Milne G.A., 2002, *Present-Day Secular Variations in the Low-Degree Harmonics of the Geopotential: Sensitivity Analysis on Spherically Symmetric Earth Models,* Journal of Geophysical Research, Vol 107, doi: 10.1029/2001JB000696

Tanaka Y., Klemann V., Martinec Z., Riva R.E.M., 2011, *Spectral-Finite Element Approach to Viscoelastic Relaxation in a Spherical Compressible Earth: Application to GIA Modeling,* Geophysical Journal International, Vol 184, doi: 10.111/j.1365-246X.2010.04854.x

Tanaka Y., Klemann V., Okuno J., 2009, *Application of a Numerical Inverse Laplace Integration Method to Surface Loading on a Viscoelastic Compressible Earth Model,* Pure and Applied Geophysics, Vol 166, doi:10.1007/s00024-009-0508-y

Tanaka Y., Okuno J., Okubo S., 2006, *A New Method for the Computation of Global Viscoelastic Post-Seismic Deformation in a Realistic Earth Model (I)-Vertical Displacement and Gravity Variation,* Geophysical Journal International, Vol 164, doi:10.1111/j.1365-246x.2005.02821.x

Tromp J. and Mitrovica J.X., 1999, *Surface Loading of a Viscoelastic Earth – II. Spherical Models,* Geophysical Journal International, Vol 137, doi:10.1046/j.1365-246x.1999.00839.x

Turcotte, D. and Schubert, J., 2002, *Geodynamics*, 2nd ed., Cambridge, UK: Cambridge University Press

Wang L., Bevis M., Peng Z., Kaban M.K., Thomas M., Chen C., 2022, *Tracking the Source Direction of Surface Mass Loads Using Vertical and Horizontal Displacements from Satellite Geodesy: A Case Study of the Inter-Annual Fluctuations in the Water Level in the Great Lakes,* Remote Sensing of Environment, Vol 274, doi: 10.1016/j.rse.2022.113001

Woodward R.J., 1888, *On the Form and Position of the Sea Level: with Special Reference to its Dependence on Superficial Masses Symmetrically Disposed About a Normal to the Earth's Surface*, United States Geological Survey, Bulletin 48, https://doi.org/10.3133/b48

Wu P., Peltier W.R., 1982, *Viscous Gravitational Relaxation*, Geophysical Journal International, Vol 70, https://doi-org/10.1111/j.1365-246X.1982.tb04976.x

Wu P. and Wang H., 2006, *Effects of Mode Coupling and Location of Rotational Axis on Glacial Induced Rotational Deformation in a Laterally Heterogeneous Viscoelastic Earth,* Geophysical Journal International, Vol 167, doi: 10.1111/j.1365-246X.2003.03103.x

Zhong S., Paulson A., Wahr J., 2003, *Three-dimensional Finite-element Modeling of Earth's Viscoelastic Deformation: Effects of Lateral Variations in Lithospheric Thickness*, Geophysics Journal International, Vol 155, 679-695, doi:10.1046/j.1365-246X.2003.02048.x